Master's thesis
Your Field

Formation of cores by merging supermassive black holes

Joonas Suortti

October 24, 2019

Tutor: prof. Smith

Censors: prof. Smith
doc. Smythe

UNIVERSITY OF HELSINKI
Department of Something

PL 42 (Kuvitteellinen katu 1)
00014 Helsingin yliopisto

"Bachelor's degrees make pretty good placemats if you get them laminated."

—Jeph Jacques

HELSINGIN YLIOPISTO — HELSINGFORS UNIVERSITET — UNIVERSITY OF HELSINKI

Tiedekunta — Fakultet — Faculty	Laitos — Institution — Department
Faculty of Whatever	Department of Something

Tekijä — Författare — Author

Joonas Suortti

Työn nimi — Arbetets titel — Title

Formation of cores by merging supermassive black holes

Oppiaine — Läroämne — Subject

Your Field

Työn laji — Arbetets art — Level	Aika — Datum — Month and year	Sivumäärä — Sidoantal — Number of pages
Master's thesis	October 24, 2019	0 pages

Tiivistelmä — Referat — Abstract

Abstract goes here.

Avainsanat — Nyckelord — Keywords

Your keywords here

Säilytyspaikka — Förvaringsställe — Where deposited

Muita tietoja — övriga uppgifter — Additional information

Contents

1. Introduction

2. Background Theory

2.1 Elliptical Galaxies

2.1.1 Basic Properties and Classification

Elliptical galaxies (Es) are galaxies characterised by their ellipsoidal shape, lack of a rapidly rotating disk, and their small or essentially non-existent cool gas and dust content. Due to the absence of star formation caused by the lack of cool gas and dust, the stellar population of elliptical galaxies is generally quite old, with a mean age of $\gtrsim$ 10 Gyr (Mo et al., 2010). This correlates well with their observed red colours (Cappellari, 2016).

Elliptical galaxies are included in the Hubble classification of galaxies (Hubble, 1926). In the Hubble "tuning-fork diagram" (*add figure for this*), they are located left of the point where the sequence diverges into the two spiral galaxy paths. This means that alongside lenticular galaxies, which are transitional objects between elliptical and spiral galaxies, elliptical galaxies are so-called "early-type galaxies" (ETGs). ETGs are, in general, often defined simply as galaxies that do not contain spiral arms.

In the Hubble classification, elliptical galaxies are further divided into seven different subcategories according to their ellipticity. These categories range from E0 to E7, where the number denotes the tenth multiple of the galaxy's ellipticity rounded to the nearest integer. The ellipticity of a galaxy is simply the measure of how flattened an observed 2D-projection of a spherical stellar system is. It can be calculated using the equation:

$$\epsilon = 1 - \frac{b}{a}, \tag{2.1}$$

where a and b parameters are the semi-major and semi-minor axes of a luminosity isophote (i.e. constant luminosity or surface brightness contour) respectively. The larger the ellipticity, the flatter the system ($\epsilon = 0$ denotes a completely spherical galaxy). It is important to note, however, that the ellipticity of a system can depend on the specific isophote from which it is calculated. Since the isophotes of elliptical galaxies generally become flatter the farther they are located from the galactic centre (Binney and Tremaine, 2008), this could result in a single galaxy having multiple ellipticities. To remedy this, the Hubble classification uses the ellipticity at the effective radius (R_e) to determine the subcategory of an elliptical galaxy. The effective radius is the radius of a sphere that encloses half of the galaxy's luminosity. Since elliptical galaxies do not have clearly defined boundaries, R_e is also often used as their measure of size.

2.1.2 Photometry

The photometric properties of elliptical galaxies are often discussed in terms of the surface brightness, i.e. the amount of observed luminosity from a unit area. Thus, an important property for studying the general spatial distribution of stellar material in the observed elliptical galaxies, is the one-dimensional radial surface brightness profile $I(R)$, where R is the projected distance from the centre of the galaxy. In practice, these profiles can be constructed by calculating the azimuthal averages of the surface brightnesses at every projected radius R (Merritt, 2013).

The observed surface brightness profiles of elliptical galaxies are smooth and featureless, falling smoothly as the projected radius grows, until the galaxy is indistinguishable from the back ground radiation (Binney and Tremaine, 2008). These observed "power-law"-like profiles are quite similar in shape across all elliptical galaxies, which has led to the formulation of a multitude of models that attempt to describe this general shape. An early example of such a model is the "de Vaucouleurs" power-law profile: $I \propto R^{1/4}$ (de Vaucouleurs, 1948). This profile, however, is quite simple, and only represents well the profiles of some elliptical galaxies, namely bright ellipticals (Merritt, 2013).

Compared to the de Vaucoulers-profile, a more robust and more prominently used model is the Sérsic-profile (Sérsic, 1968):

$$I(R) = I_e \exp\{-b_n \left[(R/R_e)^{1/n}\right]\}, \tag{2.2}$$

where R is the projected distance from the galactic centre, I_e is the surface brightness at the effective radius, n is the so-called Sérsic index ($n = 4$ gives a Sérsic profile which is identical to the de Vaucouleurs profile), and b_n is a shape factor, which is defined so that the definition of R_e holds true. The value for the shape factor can be approximated as $b_n \approx 2n - 0.324$, when $1 \lesssim n \lesssim 10$ (Binney and Tremaine, 2008). The prominent use of the Sérsic-profile is due to the fact, that it describes the observed surface brightness profiles of many different elliptical galaxies well for a large range of radii (Merritt, 2013). However, when extrapolated to the galaxies' central regions, the profile often deviates from the observations. Kormendy et al. (2009) find that there are two kinds of deviations. The galactic cores either contain "missing" or "extra" light, resulting in, what are often called, "cored" or "cuspy" central surface brightness profiles respectively.

Whether the central surface brightness profile of an elliptical galaxy is a shallow "cored" profile or a steep "cuspy" profile is seemingly tied to the absolute magnitude of the galaxy. Typically, bright ellipticals ($\mathcal{M_V} \lesssim -22$) have central profiles with missing light, while fainter galaxies ($-22 \lesssim \mathcal{M_V} \lesssim -16$) contain extra light at their centres (Kormendy et al., 2009).

This supposed dichotomy between brighter and fainter ellipticals also extends to the isophotal shapes of the galaxies. Usually the shapes of the isophotes of elliptical galaxies deviate from exact exact ellipses, and the brighter ellipticals contain so-called "boxy" isophotes, while the isophotes of the fainter galaxies are typically more "disky" (*add figure of disky and boxy isophotes*) (Mo et al., 2010). Whether the shapes of the isophotes are "boxy" or "disky", can be determined from the Fourier transformation of the deviations of the observed isophotes from perfect ellipses, using the following formula:

$$\Delta(\phi) = R_{\rm iso}(\phi) - R_{\rm ell}(\phi) = a_0 + \sum_{n=1}^{\infty}(a_n \cos(n\phi) + b_n \sin(n\phi)), \tag{2.3}$$

where $R_{\rm iso}(\phi)$ is the radius of the isophote at the angle ϕ, $R_{\rm ell}(\phi)$ is the radius of the corresponding perfect ellipse at the same angle, and where a_n and b_n are the Fourier coefficients. If $a_4 < 0$ holds true the isophote is "boxy", and if $a_4 > 0$ holds true the shape of the isophote is deemed "disky".

2.1.3 Kinematics

The divide between bright and faint elliptical galaxies, specified in the previous section, seems to also include the kinematics of the galaxies (discussed in e.g. Mo et al., 2010). The brighter galaxies rotate slowly, while the rotation of the faint galaxies is fast (Davies et al., 1983). Furthermore, the velocity distributions of the bright "boxy" galaxies are relatively anisotropic, compared to the more isotropic velocity distributions of the fainter and more disk-like, galaxies (Kormendy et al., 2009; Krajnović et al., 2008). This gives credence to the idea that the oblate shape of the fainter galaxies comes from rotational flattening, whereas the shape of the brighter galaxies is supported by their anisotropic velocity distributions.

A further distinction between the bright and relatively faint ellipticals can be drawn from their gravitational potentials. While the "disky" galaxies are assumed to be axisymmetric, the "boxy" galaxies seem to be triaxial (Mo et al., 2010). This can be seen from the fact, that unlike the fainter galaxies, bright Es often contain kinematic misalignments, i.e. the position angles of their projected kinematic axis and photometric minor axis differ from each other. According to Mo et al. (2010), these misalignments can arise as a result of two different effects. A kinematic misalignment might be caused by, a misalignment between the projected and the apparent observed minor axes of the galaxy, which can occur when observing a triaxial galaxy from nearly any viewing angle. On the other hand, the deviation in the position angles might also be the result of the observed galaxy having intrinsically misaligned angular momentum, which would be a natural consequence of triaxial potentials supporting rotation around both the short and long axis. Both of these effects require the host galaxy to be triaxial.

Slowly rotating bright ellipticals often exhibit so-called *Kinematically Distinct Cores* (KDCs). KDCs are central regions of galaxies with an angular momentum that has a different or even opposite direction when compared to the rest of the galaxy. Once again, the existence of a KDC in a galaxy might point to the host being triaxial, as they could simply be projections of major stellar families orbiting in a triaxial potential (Statler, 1991; Mo et al., 2010).

2.1.4 Formation Models

There are two main models for the formation of elliptical galaxies: the monolithic collapse scenario and the merger scenario (Mo et al., 2010). In the monolithic collapse scenario, elliptical galaxies are formed through the collapse and virialization of some initial condition, which results in the simultaneous formation of the stellar material and assembly of the galaxy. Assuming that the collapse is dissipative, the collapse model is able to reproduce features observed in actual ellipticals; however, its main problem is that it is not compatible with the current paradigm that expects a ΛCDM cosmology for the universe. The cold dark matter (CDM) cosmology assumes a hierarchical formation for observed large scale structures, where star formation and the merging of dark matter halos are still on-going processes. This is in stark contrast to the monolithic collapse scenario, where after the initial collapse, the resulting stellar system is mostly passive.

The merger scenario suggests that elliptical galaxies are formed through mergers of two or more pre-existing fully formed galaxies (Mo et al., 2010). Thus, the formation of stars and the assembly of the final galaxy are independent of each other. Since the star formation and the assembly of the galaxy are once again largely independent from each other, this formation scenario can not be reconciled completely with the ΛCDM cosmology. However, compared to the monolithic collapse scenario, the merger model has been able to reproduce a larger number of the properties seen in elliptical galaxies.

It has also been suggested that elliptical galaxies are formed through a two-phased mechanism that is a combination of both the monolithic collapse and the merging scenarios (e.g. Oser et al., 2010). According to this model, the stellar material in elliptical galaxies is initially (redshift $2 \lesssim z \lesssim 6$) accumulated through dissipative 'in-situ' formation of stars caused by cold gas flows, a process similar to the 'monolithic collapse' scenario. Afterwards ($z \lesssim 3$), the elliptical galaxies are expected to grow as a result of both minor and major galaxy mergers (i.e. the accumulated stars are formed 'ex-situ').

Since the formation models which include galaxy mergers seem to be more representative of the actual formation mechanism of elliptical galaxies, the existence of the observed photometric and kinematic dichotomy between the "core" and "cusp" galaxies has been interpreted as differences in their respective merger progenitor galaxies. Though there are multiple properties that can affect the rotational velocity of the merger remnant, such as the ratio between galaxy merger masses (Naab and Burkert, 2003), the dichotomy is usually attributed to the existence of dissipative components in the merging galaxies (Mo et al., 2010).

The fainter Es with "cuspy" central surface brightness profiles are generally thought to have been formed through dissipative mergers of gas-rich progenitor galaxies. In a gas-rich galaxy merger, the gas is expected to accumulate in the centre of the merger remnant galaxy, resulting in a starburst event (Barnes and Hernquist, 1991). This would account for the extra-light seen in the surface brightness profiles of the faint galaxies (Hopkins et al., 2008), and deepen the central gravitational potential well, causing the remnant galaxy's velocity dispersion to rise in the core regions (Barnes and Hernquist, 1996). The central accumulation of gas and the subsequent starburst event would also cause the gravitational potential of the galaxy to become more axisymmetric. As box-orbits can only occur in triaxial-potentials, this would cause these fainter elliptical galaxies to have their characteristic disk-like shapes (Naab et al., 2006).

As a contrast, the formation mechanism for the "core" galaxies is that of dissipationless "dry" mergers. The formation of massive slowly rotating galaxies is assumed to be a two-stage process, similar to the model proposed by Oser et al. (2010). Initially, the accumulation of stellar mass in "core" galaxies is driven by rapid "in-situ" star formation caused by inflows of cold gas; and afterwards, during redshift $3 > z > 0$, their growth in mass is dominated by major gas-poor ETG mergers (Naab et al., 2009). Since the massive galaxies in major galaxy mergers are expected to contain central supermassive black holes (SMBHs), it is often proposed that the "cores" in the bright ellipticals are a result of a scouring process, where the central black holes coalesce and eject stellar material from the centre of the merger remnant in complex three-body interactions.

2.2 Core Galaxies

The basic properties of core galaxies were already discussed in the previous section, however, as they are of significant importance for this thesis, it is useful discuss them in some more detail.

While the basic principle of core galaxies being galaxies with "missing" light at their centre is easy to grasp, giving an explicit definition for what exactly constitutes a core galaxy is somewhat more challenging. Core galaxies have been defined as both, galaxies that contain a central surface brightness profile with a logarithmic slope of $\gamma < 0.3$ (Lauer et al., 1995, 2007b), and as galaxies that have surface brightness profiles that are a combination of a shallow inner profile and a steep outer profile (Kormendy and Bender, 1999). However, the problem with the former definition is that Sérsic galaxies with low values for the Sérsic index n can have shallow inner profiles even when their cores do not contain a light deficit (Graham et al., 2003). Meanwhile, Dullo and Graham (2012) argue that the latter definition results in a "disconnect with the curved outer Sérsic profile". Graham et al. (2003) suggest that core galaxies should simply be defined by a deficit in the central surface brightness profile, when compared to the inward extrapolation of the outer Sérsic profile.

The size of the core is an important property of core galaxies, as its relation to the other properties of the observed galaxy can be used to derive information about the formation history of both the galaxy and the core itself. Usually the core size is determined by fitting the observed one-dimensional surface brightness profiles with some model profile that is a combination of a shallow inner power-law and a steep outer power-law. The radius at which the outer power-law changes into the the inner power-law is called the break radius (r_b), and can be equated to the radius of the core.

There are two commonly used options for modelling the surface brightness profiles. The first one is the core-Sérsic profile (Graham et al., 2003), which can be expressed using the following equation:

$$\mu(r) = \mu' \left[1 + \left(\frac{r_b}{r}\right)^{\alpha}\right]^{\gamma/\alpha} \exp\left\{-b_n \left[\left(r^{\alpha} + r_b^{\alpha}\right)/r_e^{\alpha}\right]^{1/(\alpha n)}\right\}, \tag{2.4}$$

where r_b is the break radius, γ is the logarithmic slope of the inner power-law, α controls the sharpness of the transition between the two power-laws, b_n, r_e and n are the shape factor, effective half-mass radius and the Sérsic index of the outer Sérsic profile respectively, and the normalization factor μ' is defined by:

$$\mu' = \mu_b 2^{-\gamma/\alpha} \exp\left[b_n \left(2^{(1/\alpha)} r_b/r_e\right)^{1/n}\right], \tag{2.5}$$

where μ_b is the surface brightness at the break radius.

The second option is to use the so called Nuker profile (Lauer et al., 1995):

$$\mu(r) = 2^{(\beta-\gamma)/\alpha} \mu_b \left(\frac{r_b}{r}\right)^{\gamma} \left[1 + \left(\frac{r}{r_b}\right)^{\alpha}\right]^{(\gamma-\beta)/\alpha}, \tag{2.6}$$

where r_b is once again the break radius, μ_b is the surface brightness at the break radius, β and γ are the logarithmic slopes of the power-laws inside and outside of the break radius respectively, and α once again describes the sharpness of the transition between the two slopes.

In addition to the model fitting methods, one could also estimate the size of the core by calculating the so-called "cusp radius" r_γ. The cusp radius is the distance from the centre of the galaxy, at which the logarithmic slope of the surface brightness profile equals $\gamma' = -1/2$ (Carollo et al., 1997; Lauer et al., 2007a). This distance provides an estimate for the location where the inner power-law of the profile changes into the outer power-law or Sérsic profile, and thus r_γ can be equated to the core radius.

2.2.1 Core Formation Through Black Hole Mergers

As stated before, the most prominently proposed mechanism for the formation of the cores seen in massive ETGs is ejection of stellar material due to three-body interactions between stars and merging supermassive black holes (e.g. Faber et al., 1997; Milosavljević et al., 2002; Mo et al., 2010). These SMBH merger events are expected to occur during major galaxy mergers, which, as discussed earlier, is the expected formation mechanism for bright cored ellipticals.

Merger Event

When two galaxies containing central supermassive black holes merge, the SMBHs are expected to form a coalescing binary. The SMBH merger happens in three consecutive phases: the dynamical friction phase, the three-body interaction phase, and the gravitational wave radiation phase (Merritt, 2013). In each of the three phases, a different process removes the orbital energy of the coalescing SMBHs.

During the first phase (i.e. the dynamical friction phase), the relative orbit of the central SMBHs of the merging galaxies shrinks due to the alteration of their kinetic energies, by so-called dynamical friction. Originally proposed by Chandrasekhar (1943), it is argued that stars experience a net decelerating gravitational force when moving through a population of field-stars with isotropic random velocities. This decelerating force is called dynamical friction, and it also applies to the central SMBHs in galaxy mergers, as they move through the stellar population of the galaxy merging with their host galaxy. Dynamical friction is the main mechanism which shrinks the orbit of the SMBH binary, until the black holes form a so-called "hard binary", and dynamical friction ceases to be effective in removing the orbital energy (Binney and Tremaine, 2008). The formation of a "hard binary" happens when the relative velocities of the binary black holes become much larger than the velocity dispersion of the surrounding stars. This also marks the beginning of the next phase in the SMBH merger event.

The second phase of the SMBH merger, and the phase which is assumed to cause the actual formation of the core, is the three-body interaction phase, where the orbital energy is removed from the black hole binary through the scattering of strongly interacting field-stars. These stars exchange kinematic energy with the binary, and as a result are launched out of the system. Which stars have a strong enough interaction with the SMBH binary is determined by the loss-cone, a region in phase-space (*note: phase-space will be explained in the Galactic Dynamics section*) where the angular momentum of a star fulfils the following condition:

$$L \lesssim [G(M_1 + M_2)a]^{1/2}\,, \tag{2.7}$$

where M_1 and M_2 are the masses of the binary SMBHs, and a is the semi-major axis of their orbit (Binney and Tremaine, 2008).

The transferring of kinetic energy away from the SMBH binary shrinks its orbit, and once the separation between the black holes is small enough, the gravitational wave radiation phase starts. During this phase, the radiation of gravitational energy in the form of gravitational waves becomes significant, which reduces the kinematic energy of the binary, causing its orbit to shrink further. Once enough gravitational energy has been radiated, and the orbit of the black holes has shrunk enough, the SMBHs coalesce, forming a singular black hole.

However, the binary might not even be able to get to the gravitational radiation phase of the merger. As seen in equation 2.7, the size of the loss-cone shrinks as the orbit of the binary becomes smaller. This leads to the "final parsec problem" (Milosavljević and Merritt, 2003); where, both due to its shrinking size and the ejection of mass from the loss-cone, the number of stars that can interact strongly with the binary becomes so small, that the coalescence of the SMBHs effectively ceases during the three-body-interaction phase. As the name implies, this occurs around when the semi-major axis of the binary becomes ~ 1 pc in length.

There are repopulation mechanisms which attempt to reconcile the "final parsec problem". One of such mechanisms is repopulation of the loss-cone due to two-body relaxation. However, this has been found to be too inefficient, as the relaxation time scale even at small radii is likely larger than the Hubble time (Milosavljević and Merritt, 2001). Another proposed repopulation mechanism is the secondary slingshot; where the initial interaction between the binary and an orbiting star only moves the star into another bound orbit, from which it may interact with the binary once more (Merritt, 2013). It is also possible that the triaxial geometry of the massive elliptical galaxies, where the SMBH coalescence is expected to occur, could be the answer to the problem. For example, Gualandris et al. (2017) find that collisionless orbit diffusion in triaxial potentials can account for the repopulation of the loss-cone, and even conclude that: "there is no 'final parsec problem'".

Evidence for Core Formation Through SMBH Mergers

Whether the cores of the core galaxies actually form through black hole mergers, depends on how probable the occurrence of these kind of events is. It is generally accepted that most galaxies have supermassive black holes in their center, so the idea that a galaxy merger would contain two SMBHs is not far-fetched. There have also been some observational evidence for SMBH binaries occurring in the centre of galaxies. For example, Rodriguez et al. (2006) observed two active galactic nuclei (AGN) with a projected separation of $\sim$ 7.3 pc in the galaxy NGC 6240. Since AGN are formed by accretion of material onto supermassive black holes, and since the total mass of these supposed BHs in NGC 6240 is $\sim 1.5 \times 10^8 M_\odot$, both of the AGN are inside their gravitational influence radius, and the SMBHs would thus be considered a binary. The presence of an SMBH binary has also been observed in the active galaxy OJ 287, where the periodical optical variety of the AGN has been attributed to a smaller SMBH passing through the accretion disk of the larger active black hole (Merritt, 2013).

As for the existence of black hole mergers, recent gravitational wave observations done using the *Laser Interferometer Gravitational-Wave Observatory* (LIGO, Abbott et al. 2016, 2019), provide unequivocal evidence that at least stellar-mass black hole mergers can occur. Though SMBH mergers have yet to be observed, the fact that black hole mergers have been shown to exist, alongside the aforementioned binary SMBH observations, greatly supports the idea that merging supermassive black holes could play a part in the evolution of some galaxies.

The relation between the observed cores and black holes has also been observed. Both simulations and observations have shown that a relation between the central SMBH mass ($M_\bullet$) and the quantity of the observed mass deficit ($M_{\rm def}$) exists (Graham, 2004; Merritt, 2006; Dullo and Graham, 2014). Furthermore, there seems to be a relation between the mass of the SMBH and the radius of the depleted core. Dullo and Graham (2012), for example, derive the following two possible scaling relations using different methods:

$$\log\left(\frac{r_b}{\rm pc}\right) = (1.03 \pm 0.20)\log\left(\frac{M_\bullet}{10^9\ M_\odot}\right) + (2.08 \pm 0.22), \tag{2.8}$$

and

$$\log\left(\frac{r_b}{\rm pc}\right) = (1.45 \pm 0.29)\log\left(\frac{M_\bullet}{10^9\ M_\odot}\right) + (2.03 \pm 0.16). \tag{2.9}$$

Clearly, the mass of the central SMBH is tightly connected to the properties of the core.

Though not necessarily proving that the formation of the central SMBH is connected to the development of the core, further evidence that the central black hole is inherently linked to the properties of its host galaxy can be seen in the three main scaling relations of the SMBH mass. These relations, as given by Merritt (2013), include the $M_\bullet - \sigma$ relation:

$$\frac{M_\bullet}{10^8\ M_\odot} = (1.66 \pm 0.24)\left(\frac{\sigma}{200\ {\rm km\,s^{-1}}}\right)^{(4.86 \pm 0.43)}, \tag{2.10}$$

where σ is the velocity dispersion; the $M_\bullet - L_{\rm bulge}$ relation:

$$\log_{10}\left(\frac{M_\bullet}{M_\odot}\right) = (1.13 \pm 0.12)\log_{10}\left(\frac{L_{\rm K,bulge}}{L_{\rm K,\odot}}\right) + (8.21 \pm 0.07), \tag{2.11}$$

where $L_{\mathrm{K,bulge}}$ is the luminosity of the galactic bulge in K-band magnitudes; and the $M_\bullet - M_{\mathrm{bulge}}$ relation:

$$\log_{10}\left(\frac{M_\bullet}{M_\odot}\right) = (0.96 \pm 0.07)\log_{10}\left(\frac{M_{\mathrm{bulge}}}{M_\odot}\right) + (8.28 \pm 0.06), \qquad (2.12)$$

where M_{bulge} is the mass of the central bulge. These three relations have often been used as evidence, for the coevolution of the central black holes and their host galaxies. However, it is debatable whether this coevolution actually exists (Kormendy and Ho, 2013).

2.3 Integral-Field Spectroscopy

Integral-field spectroscopy (IFS) has become an essential part of studying the kinematic properties of ETGs, as it allows for the spatial analysis of galactic spectra. IFS is done using instruments called "integral-field units", which, in principle, calculate the spectrum of the observed light for each pixel. However, often the signal-to-noise ratio (S/N) of singular pixels is quite poor. To improve the S/N, the pixel measurements are usually combined into so-called "spaxels" (i.e. spatial pixels) using an algorithm, such as the Voronoi-tessellation algorithm (Cappellari and Copin, 2003). This results in IFU-maps similar to figure (find some figure to show).

By creating a histogram out of the observed velocities in the pixels forming a spaxel, the spaxels can show the line-of-sight velocity distribution (LOSVD) of the regions in the observed galaxy that they encompass. The analysis of the LOSVDs is done by fitting the velocity histogram with some theoretical distribution function. Since the LOSVDs are rarely purely Gaussian (Mo et al., 2010), quite often (e.g. the SAURON and ATLAS$^{3\mathrm{D}}$ projects, as well as the MASSIVE survey; Bacon et al. 2001; Cappellari et al. 2011; Ma et al. 2014) the fitted distribution function is the following form of the modified Gaussian function (van der Marel and Franx, 1993;

Bender et al., 1994):

$$f(v) = I_0 e^{-\gamma^2/2}(1 + h_3 H_3(y) + h_4 H_4(y)), \tag{2.13}$$

where I_0 is a normalization constant, γ is the central slope of the particle density profile, $y = (v - V_{\mathrm{avg}})/\sigma$, and H_3 and H_4 are the third and fourth order Hermite polynomials respectively:

$$H_3(y) = \left(2\sqrt{2}y^3 - 3\sqrt{2}y\right)/\sqrt{6}, \tag{2.14}$$

$$H_4(y) = \left(4y^4 - 12y^2 + 3\right)/\sqrt{24}. \tag{2.15}$$

The four remaining parameters: the average LOS velocity V_{avg}, the LOS velocity dispersion σ, and the third and fourth order Gauss-Hermite moments h_3 and h_4, which represent skewness and kurtosis respectively, are usually the parameters that are of interest.

By using IFS, a number of different kinematic features have been found in ETGs. In general, depending on the observed galaxy, IFU-maps can be either single component (SC) or multiple component (MC) maps, where MC maps have abrupt and significant changes in the position angle of the kinematic axis of the galaxy, while the potential changes in the direction of the kinematics of SC maps are more gradual (these gradual changes are also called "kinematic twists") (Krajnović et al., 2006, 2011). These observed kinematic components then exhibit several behaviours themselves, such as low-level velocities, disk-like rotation and kinematic misalignment (Emsellem et al., 2007). IFS has also helped identify KDCs, and their more extreme counterparts *Counter Rotating Cores* (CRCs), which are central regions of galaxies that have a difference of around 180° in their kinematic position angle, when compared to their immediate surroundings (Krajnović et al., 2011).

Slow and Fast Rotators

Relating to the dichotomy between ellipticals with slow and fast rotation discussed in the section 2.1.3; with IFS, it is possible to make a definitive distinction between the two types of rotators using quantitative measurements of LOS velocities (Emsellem et al., 2007). This is done using the λ_R parameter, which describes the angular momentum of a galaxy, and is defined as:

$$\lambda_R \equiv \frac{\langle R|V|\rangle}{\langle R\sqrt{V^2+\sigma^2}\rangle}, \tag{2.16}$$

where R is the projected distance from the galactic centre, V is the line-of-sight velocity, σ is the velocity dispersion and $\langle\ \rangle$ denote that the nominator and denominator in the equation are luminosity weighted means. From binned 2D kinematic maps, such as the ones given by IFS observations, this property can be calculated using the following formula:

$$\lambda_R = \frac{\sum_{i=1}^{N_p} F_i R_i |V_i|}{\sum_{i=1}^{N_p} F_i R_i \sqrt{V_i^2+\sigma_i^2}}, \tag{2.17}$$

where F_i, R_i, V_i and σ_i are the flux, projected distance from the galaxy centre, velocity and velocity dispersion of the ith bin, and N_p is the number of bins.

Determining whether a galaxy is a fast or a slow rotator using λ_R, is done by comparing the value that the parameter gets at the galaxy's effective radius, to some pre-defined threshold. The originally used threshold is: $\lambda_{Re} < 0.1$, where λ_{Re} is the aforementioned λ_R at the effective radius, and where galaxies fulfilling this condition are classified as slow rotators (Emsellem et al., 2007). A revision of the threshold by Emsellem et al. (2011) takes the ellipticity (ϵ) of the galaxy into account, and defines slow rotators as having $\lambda_{R_e} < 0.31\sqrt{\epsilon}$, which accounts for the increased anisotropy in the kinematics of flatter galaxies. An even further refinement of the slow rotator definition has been proposed by Cappellari (2016), where slow rotator galaxies are determined using the following two criteria: $\lambda_{R_e} < 0.08 + \epsilon/4$ and $\epsilon < 0.4$. The former criterion of the threshold reduces the risk of misidentifying very round non-regular slow rotators as fast rotators, while the latter makes sure that only sufficiently round galaxies are classified as slow rotators (Cappellari 2016 argues that "genuine" disk-less slow rotators are all rounder than $\epsilon = 0.4$).

Slow rotator galaxies, when defined using the above methods, often contain a KDC, and usually exhibit: anisotropic velocity distributions, little to no large-scale rotation, kinematic misalignments and twists (Emsellem et al., 2007; Cappellari et al., 2007). In contrast, the velocity distributions of fast rotators are isotropic and their kinematic axis is aligned closely with their photometric axis (Emsellem et al., 2007). They also have disk-like kinematics and nearly oblate shapes (Cappellari et al., 2007).

As expected, the dichotomy between slow and fast rotators clearly mirrors the kinematic differences between "boxy" and "disky" ellipticals. This implies that the cored and coreless galaxies should follow the slow and fast rotator divide as well. Krajnović et al. (2013) find that this does seem to be the case, however there are a few exceptions. Nevertheless, even when accounting for these exceptions, Cappellari (2016) for example, consider the agreement broad enough, that it is possible to adequately draw conclusions about the photometry or kinematics of these galaxies.

2.4 Galactic Dynamics

2.4.1 Potential-Density Models

The majority of the movement inside a galaxy is caused by gravitational forces. Thus, knowledge about the gravitational potential of a stellar system is fundamental when studying its internal dynamics. The naive way of calculating the total potential of the galaxy, would be to sum the point-mass potentials of every single object with mass together. Unsurprisingly, this is usually not feasible, simply due to the sheer number of such objects in large scale systems. Thus, objects inside a galaxy are expected to move through a smooth mass-density distribution, the gravitational potential of which can be calculated using the Poisson equation (Binney and Tremaine, 2008):

$$\nabla^2\phi = 4\pi G\rho, \tag{2.18}$$

where ϕ is the gravitational potential, G is the gravitational constant, and ρ is the mass-density distribution.

In simulations of galactic dynamics, the density distribution in equation 2.18 is usually calculated using some numerical method, after which the gravitational potential can be determined using so-called "Poisson solvers" (e.g. section *Refer to Poisson solver used in KEJTU and described in chapter 3*). Analytically, however, the smoothed density of the galaxy has to be assumed. This leads us to the "potential-density models", where galaxies are modelled using a mass-density distribution and the corresponding gravitational potential. The gravitational potential is often calculated from the density using the Poisson equation, although in the case of some models (e.g. "Plummer" and "Kuzmin" models, Binney and Tremaine 2008), this is reversed, and the density is calculated from the potential.

One of the most popular potential-density models used when approximating elliptical galaxies, is the spherically symmetric Dehnen-model (Dehnen, 1993), which is defined as:

$$\rho(r) = \frac{(3-\gamma)M}{4\pi}\frac{a}{r^{\gamma}(r+a)^{4-\gamma}}, \tag{2.19}$$

$$\phi(r) = \frac{GM}{a} \times \begin{cases} -\frac{1}{2-\gamma}\left[1-\left(\frac{r}{r+a}\right)^{2-\gamma}\right] & \gamma \neq 2 \\ \ln\frac{r}{r+a} & \gamma = 2 \end{cases}, \tag{2.20}$$

where M is the total mass, a is the scaling radius, and γ is the central slope of the profile. There are a few reasons why this model in particular is used often. Firstly, the density profile is a combination of two power-laws. This is similar to many observed luminosity and surface brightness profiles in Es (see section 2.1.2), and also many simulated dark-matter profiles (Binney and Tremaine, 2008). Furthermore, when projected, the outer parts of the density profile resembles the empirical "de Vaucouleurs" surface brightness profile. The model is also a generalization of two other commonly used potential-density models, namely the Jaffe-model and the Hernquist-model (for these models $\gamma = 2$ and $\gamma = 1$ respectively Jaffe, 1983; Hernquist, 1990).

2.4.2 Collisionless Systems

2.5 Regularization

The nature of elliptical galaxy mergers and the formation of merger remnants with cores deficient in light, is such, that simulations of the process must take into account collisions between stars and black holes. This leads to a common issue encountered in simulations of collisional systems, namely the singularity at $r = 0$ in the equation of motion (Binney and Tremaine, 2008):

$$\ddot{r} = -GM/r^2, \tag{2.21}$$

where G is the gravitational constant, M is the total mass of the two interacting particles, and r is the distance between the particles. Often, in order to maintain accuracy in situations where large changes in the simulated system can occur in small time-frames, the integrators used in large-scale merger simulations, reduce the length of the time-steps when particles get close to the aforementioned singularity. However, this raises a problem, where, as the particles get closer to each other, the time steps become so small that the simulation time effectively stops progressing.

The solution to the above issue is so-called regularization, where the singularity in the equation of motion (equation 2.21) is removed through a coordinate transformation. Two examples of such transformations are given by Binney and Tremaine (2008). The first is the "Burdet-Heggie regularization", which adds the gravitational field of the other particles to the two-body problem, and changes the simulation time to the fictitious time: $\mathrm{d}t = r\ \mathrm{d}\tau$. However, as will become apparent in the next chapter, of more importance to us is the second coordinate transformation, i.e. the "Kustaaheimo-Stiefel" (KS) regularization.

Like the Burdet-Heggie regularization, the KS-regularization procedure defines a new fictitious time $\mathrm{d}t = r\ \mathrm{d}\tau$ and adds the gravitational field of the other particles to the equation of motion. However, KS-regularization also makes a positional coordinate transformation by changing the position vector $\mathbf{r} = (x, y, z)$ into a corresponding four-vector $\mathbf{u} = (u_1, u_2, u_3, u_4)$, where:

$$\begin{aligned} u_1^2 &= \frac{1}{2}(x+r)\cos^2\psi \\ u_2^2 &= \frac{yu_1 + zu_4}{x+r} \\ u_3^2 &= \frac{zu_1 + yu_4}{x+r} \\ u_4^2 &= \frac{1}{2}(x+r)\sin^2\psi, \end{aligned} \tag{2.22}$$

and where ψ is some arbitrary parameter. If ϕ_e is the gravitational potential induced outside the particles outside the two-body problem, the equation of motion becomes as follows:

$$\mathbf{u}'' - \frac{1}{2}E\mathbf{u} = -\frac{1}{4}\frac{\partial}{\partial \mathbf{u}}\left(|\mathbf{u}|^2\phi_e\right), \tag{2.23}$$

where $\mathbf{u}''$ denotes the second fictional time derivative of the four-vector, and E is the energy of the two-body orbit when ϕ_e is taken into account:

$$E = \frac{1}{2}v^2 - \frac{GM}{r} + \phi_e = 2\frac{|\mathbf{u}'|^2}{|\mathbf{u}|} - \frac{GM}{|\mathbf{u}|^2} + \phi_e. \tag{2.24}$$

As equation 2.23 clearly shows, the regularized form of the equation of motion is well defined even when the new position vector gets the value $\mathbf{u} = 0$, and thus does not contain the same singularity as the basic Cartesian version in equation 2.21.

Figure (*take figure from Binney*) by Binney and Tremaine (2008) compares the fractional errors in the energies of highly eccentric simulated orbits ($e = 0.99$), integrated in differently regularized (or non-regularized) coordinates, after one pericenter passage. The figure clearly shows how important the removal of the singularity is for the accuracy of the integration of the orbit. In regularized coordinates, the integrators require around an order of magnitude less force evaluations to achieve the same accuracy than in unregularized coordinates. Furthermore, the efficiency of the integration seems to also be affected by the type of regularization, as the more robust KS-regularization results in a smaller fractional energy error as the Burdet-Heggie regularization.

2.6 Post-Newtonian Dynamics

3. KETJU

Description of basic functionality: what KETJU does, why it's created, basic description of the multiple integration region system.

3.1 AR-CHAIN / Chain Integrator

Chain forming, force calculations, integration

3.2 GADGET-3 / Tree Integrator

Softening, tree-codes, calculations

3.3 Combined Functionality

How the AR-CHAIN and GADGET-3 integrators work together: time-step problem, tidal-perturbations, particles moving from one region to another, chain macro-particle

3.3.1 Particle Types

Chain particles, tree particles, perturber particles

3.4 Merging of Black Hole Particles

Since we are trying to determine if merging SMBH binaries form cores in merger remnants, we must make sure that the progenitors' central black holes actually merge in our simulations. This is done by looking at the "Run" simulations, as they contain the locations of the black holes from multiple time steps, and as the "Snapshots" still show both of the SMBHs.

Plotting the positions of the black holes from "Run 3" in coordinates centred on the binary's centre-of-mass during the initial time step gives us figure 3.1. Even by eye, one can clearly see that the orbit of the black hole with a smaller mass becomes smaller and smaller as the binary moves further away from its initial position. While this doesn't explicitly tell us that the black holes merge into each other, it does indicate the existence of a hardening process in the binary. Similar figures to figure 3.1 from all four "Runs" can be found in the appendix (figure A.1).

The most likely obstacle for the complete merging of the binary black holes is the so-called final-parsec problem; where, due to the lack of stellar material that can be ejected during the three-body scattering phase, the hardening of the binary stops when the separation between the two black holes is $\sim$ 1pc. This is assumed to happen since, not only is the binary constantly ejecting the finite amount of stars inside the loss-cone (defined in section 2), but the loss cone itself is becoming smaller due to the contracting binary orbit.

Figure 3.2 shows the time evolution of both the semi-major axis and the eccentricity of the binary orbits from all of the simulation runs. Interestingly enough the semi-major axes of all of the binaries go far below single parsec scales, meaning that the final-parsec problem doesn't seem to play a part in the simulations. This implies that, there exists some loss-cone refill mechanism which allows the binary to eject more stellar material than what initially exists inside the loss cone.

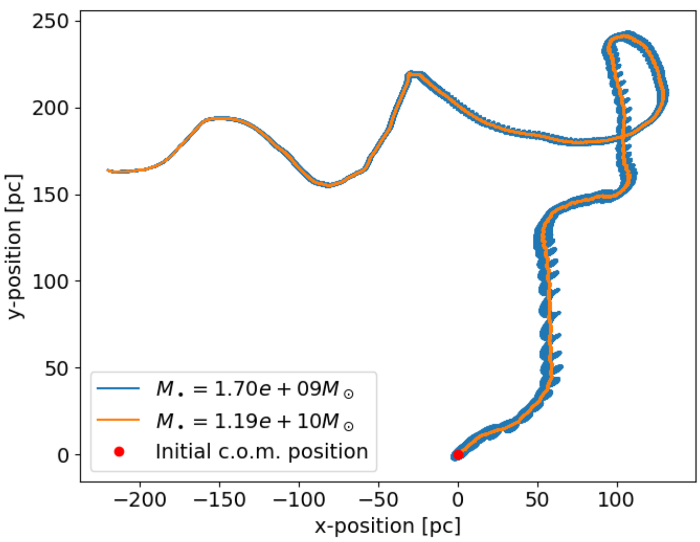

Figure 3.1: The trajectories of the black holes during "Run 3". The coordinates are centred on the initial location of the centre-of-mass of the binary black hole. The orange and blue lines show the paths taken by the smaller and larger black holes respectively. Both paths show clear spiral patterns which become smaller and smaller as the simulation proceeds. The paths end at the location where the black holes merge, i.e. where the distance between them is $\lesssim 100 R_s$ (R_s is the Schwarzschild radius).

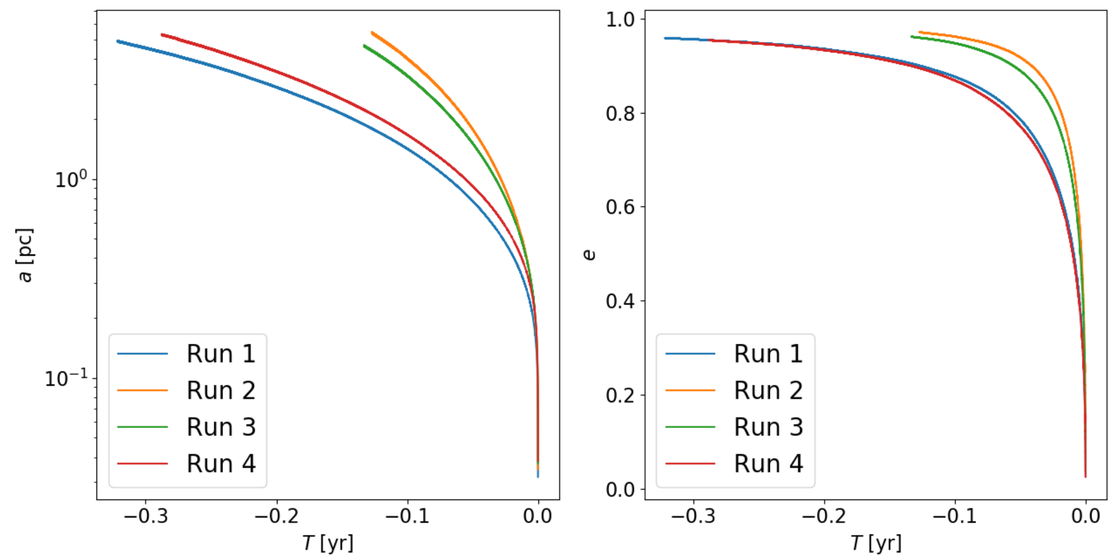

Figure 3.2: The semi-major axes (left) and eccentricities (right) of the black hole systems in the simulations "Runs 1"-"Run-4" as a function of time. The zero position on the x-axis corresponds to the point in simulation time, where the black hole merging event occurs.

4. Merger Simulations Using KETJU

In this chapter I study the formation of cored galaxies in galaxy mergers. The analysis focuses on the results from galaxy merger simulations run by Rantala et al. (2018) using the KETJU code. In all but one simulation, the merger progenitor galaxies contain central supermassive black holes. During the merger event the SMBHs form a hard binary. These binaries are a likely source for the observed low-luminosity cores, as they can eject stars from the galactic centre through complex three-body interactions. Here I determine if there is a connection between the central binary SMBH and the existence of a core deficient in light, and if the simulated KETJU results agree with observations of cored galaxies.

4.1 Simulation Details

The simulation sample run by Rantala et al. (2018) includes seven different equal-mass mergers of two identical galaxies. The merger progenitor galaxies (named BH-0 - BH-6) used in the different simulations consist of equal mass stellar particles and equal mass dark matter particles, where the mass of the stellar particles differ from the mass of the dark matter particles. The progenitors are gas free (i.e. the simulations describe so-called "dry" mergers), and all of them but one contains an SMBH at their centre.

The initial conditions (ICs) of the merger progenitor galaxies are modelled as multicomponent, spherically symmetrical stellar systems. They consist of the three aforementioned components: stellar particles, dark matter particles and a central SMBH. The central SMBH is simply modelled as a single point mass, and is located at the origin of the host galaxy's internal coordinate systems. The stellar and dark matter component, on the other hand, consist of multiple particles which are distributed according to the spherically symmetric Dehnen density-potential model defined as (Dehnen, 1993):

$$\rho(r) = \frac{(3-\gamma)M}{4\pi}\frac{a}{r^{\gamma}(r+a)^{4-\gamma}}, \tag{4.1}$$

$$\phi(r) = \frac{GM}{a} \times \begin{cases} -\frac{1}{2-\gamma}\left[1-\left(\frac{r}{r+a}\right)^{2-\gamma}\right] & \gamma \neq 2 \\ \ln\frac{r}{r+a} & \gamma = 2 \end{cases}, \tag{4.2}$$

where M is the total mass, a is the scaling radius, and γ is the central slope of the profile. For stellar particles we set $\gamma = 3/2$, while for the dark matter particles the value of $\gamma = 1$ is used ($\gamma = 1$ corresponds to the so-called Hernquist profile, Hernquist 1990). The Dehnen density-potential model uses a density profile, which is a generalization of stellar density models that, when projected, resemble the de Vaucouleurs - profile ($\log(\mu) \propto R^{1/4}$; de Vaucouleurs, 1948) in the outer parts. The model's gravitational potential profile is derived from the density profile using the Poisson equation *(refer to equation from chapter 2).*

When constructing the multicomponent ICs for the progenitor galaxies, the positions of the stellar and dark matter particles are determined through their respective cumulative mass profiles. These mass profiles are derived using the aforementioned Dehnen density-potential model, and can be written as:

$$M(r) = 4\pi\int_0^r \rho(r)r^2\,dr = M\left(\frac{r}{r+a}\right)^{3-\gamma}, \tag{4.3}$$

where $\rho(r)$ is the density profile from equation 2.19.

In equation 4.3, the value of the scaling radius (a) is determined quite differently for the stellar and dark matter particle distributions. One way of calculating a is to derive the formula for the half-mass radius from the cumulative mass profile. This gives us the equation:

$$r_{1/2} = a \left(2^{1/(3-\gamma)} - 1\right)^{-1}, \tag{4.4}$$

from which a can be solved easily. However, in order to get a value for a, one now needs to know the half-mass radius of the particle distribution. Fortunately, the half-mass radius of the stellar population can be determined through drawing an equivalence between it and the effective radius of the galaxy. If the galaxy for which we are trying to determine the scaling radius has a constant mass-to-light ratio, its mass and light profiles are proportional to each other. In this case, both profiles describe the same property, which means that the half-mass radius and the effective radius are equivalent to each other. In cases, such as our simulations, where only the 2D projection of the effective radius is known, the three dimensional half-mass radius can be approximated using the following formula:

$$R_e \approx \frac{3}{4} r_{1/2}, \tag{4.5}$$

where R_e is the aforementioned 2D projected effective radius. Thus, knowing the effective radius of the galaxy allows one to determine the stellar scaling radius $a_\star$, by using both equation 4.4 and 4.5.

The scaling radius of the dark matter particle distribution can be derived using the dark matter fraction (f_{DM}) inside the stellar half-mass radius. The dark matter fraction describes the fraction of the total mass inside radius r that is contributed by dark matter, and is defined by the following equation:

$$f_{\mathrm{DM}}(r) = \frac{M_{\mathrm{DM}}(r)}{M_\star(r) + M_{\mathrm{DM}}(r)}. \tag{4.6}$$

With the above equation, one can get the dark matter scaling radius by substituting the cumulative mass profiles in the equation with the one from equation 4.3 when

$r = r_{1/2}$, and using equation 4.4 to define the stellar half-mass radius. This gives us the following formula for calculating the dark matter scaling radius:

$$a_{\mathrm{DM}} = r_{1/2}\left[\sqrt{\frac{2M_{\mathrm{DM}}}{M_\star}\left(\frac{1}{f_{\mathrm{DM}}(r_{1/2})}-1\right)}-1\right]. \tag{4.7}$$

Finally, applying the half-mass radius approximation from equation 4.5 allows us to calculate the dark matter scaling radius as follows:

$$a_{\mathrm{DM}} \approx \frac{4}{3}\left[\sqrt{\frac{2M_{\mathrm{DM}}}{M_\star}\left(\frac{1}{f_{\mathrm{DM}}(r_{1/2})}-1\right)}-1\right]R_e. \tag{4.8}$$

If the positions of the particles in the simulated progenitor galaxies are known, their velocities can be determined using Eddington's formula (Binney and Tremaine, 2008). The different particles thus have the following distribution function in the position-velocity phase-space:

$$f_i(\varepsilon) = \frac{1}{\sqrt{8}\pi^2}\int_{\Phi_T=0}^{\Phi_T=\varepsilon}\frac{d^2\rho_i}{d\Phi_T^2}\frac{d\Phi_T}{\sqrt{\varepsilon-\Phi_T}}, \tag{4.9}$$

where ρ_i is the density profile from equation 2.19 for the particle in question, and Φ_T is the total gravitational potential ($\Phi_T = \Phi_\star + \Phi_{\mathrm{DM}} + \Phi_\bullet$). The variable ε is the relative energy:

$$\varepsilon = -\Phi_T + \Phi_0 - \frac{1}{2}v^2, \tag{4.10}$$

where v is the velocity of the particle, and Φ_0 is a chosen zero point for the potential. This zero point is usually chosen so that, $f > 0$ for $\varepsilon > 0$, and that $f = 0$ for $\varepsilon \leq 0$. In the case of our simulations the zero point is set as $\Phi_0 = 0$, since the galaxies are modelled in isolation, and extend in principle to infinity.

The general procedure for generating the multicomponent ICs of the progenitor galaxies is as follows. The positions of the stellar and dark matter particles are generated using the inverse of their respective cumulative mass function described in equation 4.3. Afterwards, using equation 4.9, values of the two particle types' distribution functions are calculated into a lookup table. The velocities of the particles are then sampled by interpolating these tabulated distribution function values. Finally, the central SMBH is placed in the centre of the progenitor galaxy.

The physical parameters needed for generating the progenitor galaxies using the aforementioned procedure are given in table 4.1 under "Common physical properties". As the name implies, they are identical across every progenitor galaxy used in the simulations; meaning that, as far as their stellar and dark matter particle populations go, the progenitors are identical.

The values for these common properties are motivated by observations and dynamical simulations of NGC 1600 (Rantala et al., 2018). NGC 1600 is a massive ($M_\star \approx 8.3 \times 10^{11} M_\odot$) early-type cored galaxy with a large observed core radius ($r_b \approx$ 2.15 arcsec, which corresponds to a physical length of $\sim$ 0.667 kpc at the distance of 64 Mpc) and a central supermassive black hole with a mass of $\sim 1.7 \times 10^{10} M_\odot$ (Thomas et al., 2016). Using the values given in table 4.1 for the physical properties of the simulated merger progenitors, the resulting merger remnant should in principle be as similar as possible to NGC 1600.

Figure 4.1 shows an example of what the stellar mass density profiles of the merger progenitors used in the simulation look like. The profile is calculated from a stellar particle distribution produced using the multicomponent IC generation procedure described previously in this section. The physical properties used in the generation of the distribution are mostly the same as the ones seen in table 4.1. The only difference being that the number of stellar and dark matter particles is only 10% of the values seen in the table. The density profile itself is calculated by moving the stellar particles of the progenitor galaxy into their centre-of-mass coordinates, dividing them into logarithmic bins, and calculating the mass density inside the respective bins.

Table 4.1 also shows the masses of the central SMBHs in each of the seven progenitor galaxies. The mass of the central SMBH is the only physical property that changes from one progenitor to another. Six of the progenitor galaxies (BH-1 - BH-6) contain central supermassive black holes, with the SMBH masses varying

Common physical properties						
$M_\star$	R_e	$M_{\rm DM}$	$f_{\rm DM}(r_{1/2})$	$N_\star$	$N_{\rm DM}$	
$[\times 10^{10} M_\odot]$	[kpc]	$[\times 10^{10} M_\odot]$				
41.5	7	7500	0.25	4.15×10^6	1.0×10^7	
$M_\bullet$ $[\times 10^9 M_\odot]$						
BH-0	BH-1	BH-2	BH-3	BH-4	BH-5	BH-6
-	0.85	1.7	3.4	5.1	6.8	7.5

Table 4.1: Physical properties of the different progenitors used in the simulations by Rantala et al. (2018).

$M_\star$: Stellar mass

R_e: 2D projected Effective radius

$M_{\rm DM}$: Dark matter halo mass

$f_{\rm DM}(r_{1/2})$: The fraction of dark matter mass from the total mass inside the half-mass radius

$N_\star$: Number of stellar particles

$N_{\rm DM}$: Number of dark matter particles

$M_\bullet$: Central SMBH Mass

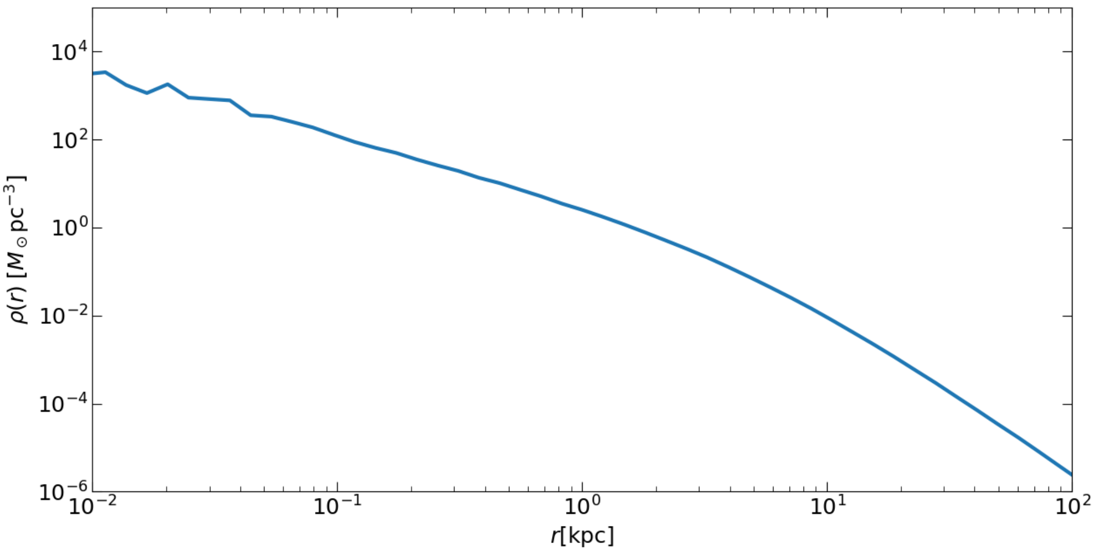

Figure 4.1: Example mass density profile of the progenitor galaxies. The initial conditions for the profile in question were the same as in table 4.1; with the exception of the number of dark matter and stellar particles, which were only 10% of their respective values. The noise in the left-side of the profile is caused by this low particle sample.

from $8.5 \times 10^8 M_\odot$ to $8.5 \times 10^9 M_\odot$. A merged binary of two of the largest SMBHs in the table, is equivalent in mass to the observed central SMBH in NGC 1600. The seventh progenitor (BH-0) does not contain an SMBH in its centre, and is included simply for the sake of comparison.

The simulations themselves thus comprise of seven mergers of two identical progenitor galaxies from table 4.1. The galaxies are merged on a nearly parabolic orbit with an initial separation of $d = 30$ kpc. This kind of orbit makes the approach of the galaxies swift, and causes the stellar cusps to merge before $t \sim 300$ Myr.

The simulation data that I will be analysing, comes in the form of snapshots of the merger remnants. These snapshots are taken at the simulation time of $\sim$ 2Gyr. At this point the progenitor galaxies have merged into a single merger remnant, however, the progenitors' central SMBHs have not yet merged and still exist in the form of a central binary. The snapshots contain the positions, velocities and masses of every particle.

4.2 Core Size Measurements

In order to test if a galaxy is cored, I calculate its surface brightness profile and check if the centre of the galaxy is deficient in light.

The surface brightness profiles are calculated from the merger remnant snapshots using the following procedure. First, the coordinate system is changed to centre-of-mass coordinates, and the stellar particles are projected onto a 2D plane. Next, we calculate the mass inside logarithmically spaced radial bins, and get a radial surface mass density profile. This is repeated 100 times from random viewing angles, which naturally results in 100 slightly different density profile projections. These profiles are then averaged azimuthally, which results in a smooth surface mass density profile. Finally, by assuming a mass-to-light ratio for the stellar particles, the surface mass density profile can be turned into a surface brightness profile (Rantala et al., 2018).

Determining the mass-to-light ratios of the stellar particles in the simulated merger remnants is problematic, as the simulations do not contain information about their ages and metallicities. The only properties that the stellar particles have are their position, velocity, and a mass that is identical for all of them; which are not enough to make valid, physically accurate, assumptions on their specific mass-to-light ratios. For this reason, a constant mass-to-light ratio of $M/L = 4$ is used. This is equivalent to the ratio derived from dynamical modelling of NGC 1600 by Thomas et al. (2016). Thus, the use of this particular M/L in the analysis of the simulation results, fits in well with the already established desire of similarity between the physical properties of the simulated merger remnants and NGC 1600.

Figure 4.2 shows the surface brightness profiles of every simulated merger remnant. Studying the curves, one can already see that, the presence of central

SMBHs in the merger progenitors causes a clear brightness deficiency near the centre of the merger remnant. In addition, there is a systematic effect which shows that the larger the mass of the central black hole binary, the larger the amount of missing light in the core.

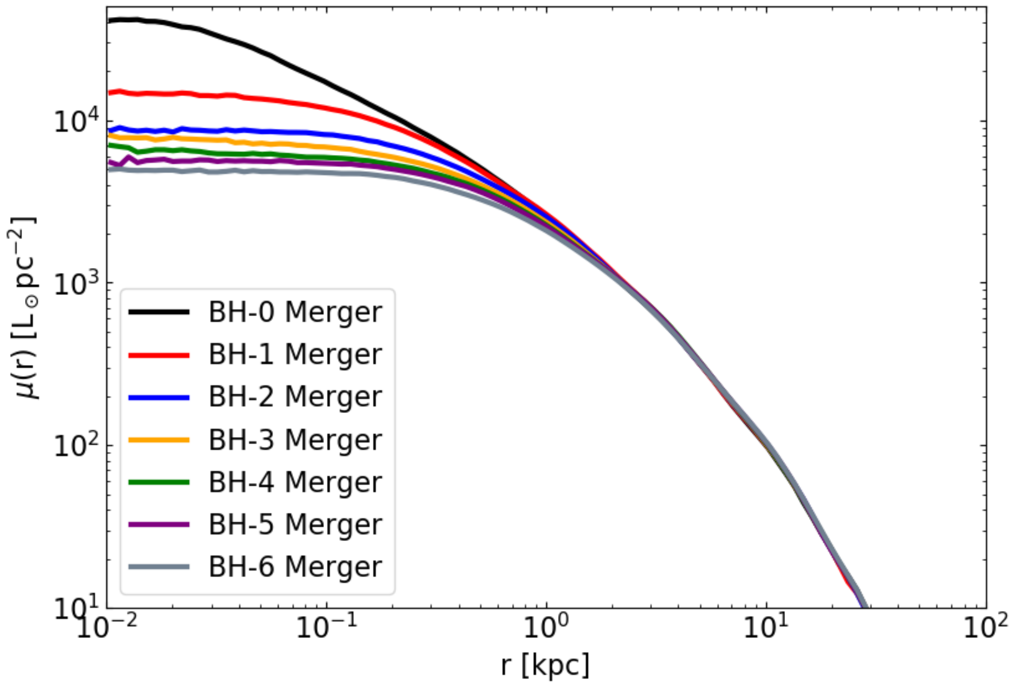

Figure 4.2: Surface brightness profiles from every simulated merger remnant. These were calculated by dividing the stellar particles in the simulated galaxy remnants into 100 radial logarithmic bins, and averaging the surface brightnesses inside these bins through 100 random viewing angles. The luminosity of the particles was estimated by assuming a constant mass-to-light ratio of $M/L = 4$.

The lack of light in the surface brightness profiles reveals the presence of cores; however, determining the precise sizes of the cores requires us to find the exact locations where the deviations from the Sérsic fit begin. This can be done by fitting the derived brightness profile with a model that is a combination of two power laws: a shallow inner power-law, and a steeper outer power-law. The radius at which the outer power-law changes into the inner power-law (and vice-versa) is called the break radius (r_b), and can be defined as the radius of the core.

There are two commonly used options for modelling the surface brightness profiles. The first one is the core-Sérsic profile (Graham et al., 2003), which can be expressed using the following equation:

$$\mu(r) = \mu' \left[1 + \left(\frac{r_b}{r}\right)^{\alpha}\right]^{\gamma/\alpha} \exp\left\{-b_n \left[\left(r^{\alpha} + r_b^{\alpha}\right)/r_e^{\alpha}\right]^{1/(\alpha n)}\right\}, \tag{4.11}$$

where r_b is the break radius, γ is the logarithmic slope of the inner power-law, α controls the sharpness of the transition between the two power-laws, r_e and n are the effective half-mass radius and the Sérsic index of the outer power-law respectively, and the normalization factor μ' is defined by:

$$\mu' = \mu_b 2^{-\gamma/\alpha} \exp\left[b_n \left(2^{(1/\alpha)} r_b/r_e\right)^{1/n}\right], \tag{4.12}$$

where μ_b is the surface brightness at the break radius.

The second option is to use the so called Nuker profile (Lauer et al., 1995):

$$\mu(r) = 2^{(\beta-\gamma)/\alpha} \mu_b \left(\frac{r_b}{r}\right)^{\gamma} \left[1 + \left(\frac{r}{r_b}\right)^{\alpha}\right]^{(\gamma-\beta)/\alpha}, \tag{4.13}$$

where r_b is once again the break radius, μ_b is the surface brightness at the break radius, β and γ are the logarithmic slopes of the power-laws inside and outside of the break radius respectively, and α once again describes the sharpness of the transition between the two slopes.

We calculate the core radii of the merger remnants by using the "Levenberg-Marquardt" fitting algorithm to fit both the core-Sérsic model and the Nuker model to the remnants' surface brightness profiles. For the most part, the initial guesses for the fitting parameters' values in the fitting algorithm, were determined through trial-and-error, as well as knowledge of their likely order of magnitude. This was not the case for the Sérsic-index (n) of the core-Sérsic profile however. In order to reduce degeneracy between the fitting parameters, n was fixed to $n = 4$ for all core-Sérsic profile fits.

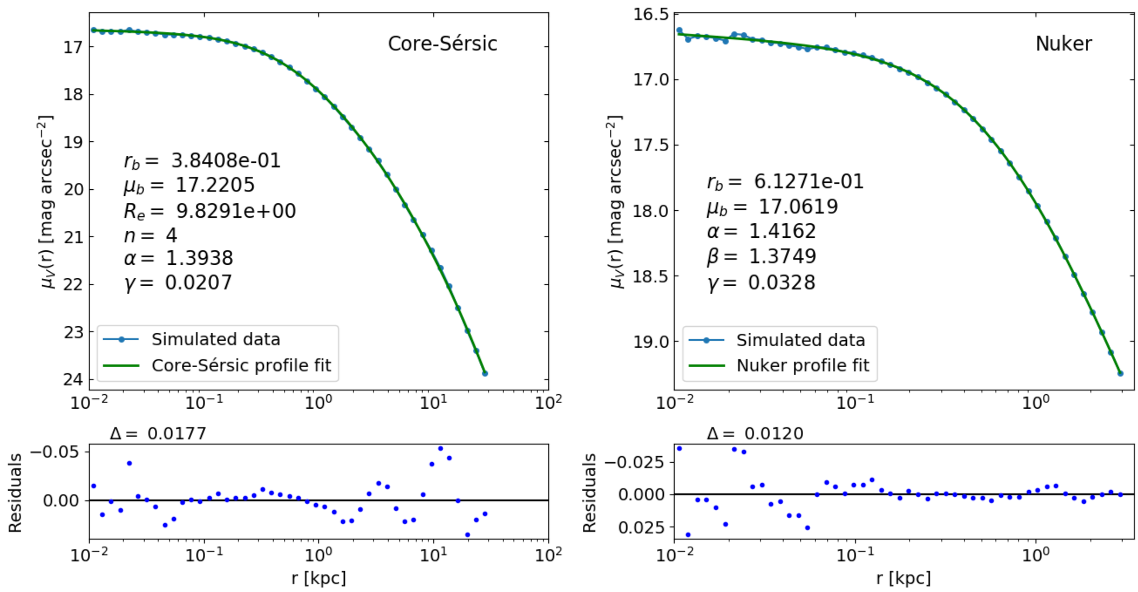

Figure 4.3: Core-Sérsic and Nuker profile fits of surface brightness profiles calculated from the BH-3 merger remnant (left and right figures respectively). The best fit parameters are shown on the figures and are in the same units as the axes (i.e. r_b and R_e in kilo-parsecs, and μ_b in V-band magnitudes per arc-second squared). The relative residuals of the fits are plotted under their respective figures. The delta describes the root-mean-square of the residuals.

Figure 4.3 shows a comparison between the core-Sérsic and Nuker profile fits for the BH-3 merger (refer to table 4.1), while figures 4.4 and 4.5 show these fits for every simulated remnant containing an SMBH binary. The values of the best-fit parameters are shown on the figures. The units of the surface brightness are changed from $L_\odot$ pc^{-2} to mag arcsec^{-2} (where mag is the magnitude in the V-band) using the common conversion formula:

$$\mu = M_\odot + 21.572 - 2.5\log(I), \tag{4.14}$$

where $M_\odot$ is the absolute magnitude of the Sun in a specific spectral band (in our case the V-band magnitude of 4.83 is used), and I is the surface brightness in $L_\odot$pc^{-2}.

The root-mean-square of the fits' residuals are comparable to the values seen in profile fits of observed surface brightness profiles: $\Delta \approx 0.02$ mag arcsec^{-2} (Dullo and Graham, 2012). Although, while the RMS of the residuals show that the fits describe the surface brightness profiles rather well, most of the fits have large residual scatter near the centre of the merger remnant. This is especially noticeable in the Nuker fits, since in order to get sensible values for the fitting parameters, the fitting range needs to be concentrated in the galactic centre (in our analysis, the fitting range used for the Nuker profile was: $\sim 0.04 - 3$ kpc, which is an order of magnitude lower compared to the range used for the core-Sérsic fit: $\sim 0.04 - 60$ kpc).

The larger central residual scatter is most likely not indicative of any kind of physical structure in the merger remnant cores; but simply a result of the logarithmic spacing of the bins in the surface brightness profiles. The bins near the centre inherently contain less particles than the outer bins. When calculating the 100 projected surface brightness profiles from random viewing angles, this causes the variations in binned luminosities to be larger in the central bins, resulting in a final averaged profile that contains small jumps as well as small dips in its central luminosity. These arbitrary inconsistencies naturally cause the residuals of the fits to be scattered in a random way near the centre of the simulated galaxy. Unfortunately, remedying this problem by using bins that have a constant number of particles did not yield satisfactory results, due to the total number of particles being extremely small near the centre.

Interestingly, all of the core-Sérsic fits show a peak in the size of the residuals at around ~ 10 kpc. Once again, this residual property is probably just a small anomaly in the simulations and not indicative of any physical structure that could be found in actual merger remnants. However, the fact that this residual anomaly appears in the surface brightness profile of every simulation, indicates that; even though the masses of the SMBHs in the merger progenitors have a large effect on the central regions of the merger remnant, the outer regions are left relatively unaffected. In fact, the central SMBH binary only affects the outer regions of the

Simulation	r_{SOI} [kpc]
BH-1 merger	0.143
BH-2 merger	0.256
BH-3 merger	0.394
BH-4 merger	0.515
BH-5 merger	0.620
BH-6 merger	0.757

Table 4.2: Estimations of the projected radii of the spheres-of-influence (r_{SOI}) for every SMBH binary. They were calculated by finding the radius of, a sphere that contains the amount of stellar mass equivalent to the mass of the binary, inside the binary's host merger remnant. The 2D projections of the radii were determined by using a relation similar to the one described in equation 4.5.

merger remnant through stellar particles that have been ejected from the galactic centre.

All of the significant residual variations between the profile fits of the simulated merger remnant galaxies are concentrated near their respective centres. This implies that the results of the different simulations vary significantly from each other only due to the formation of a central SMBH binary, since the similar shapes of the outer regions of the residual plots can be explained through the limited range of the binaries' gravitational spheres-of-influence (SOI). The sizes of the SMBH binaries' SOI can be seen in table 4.2. They were calculated by: finding the radius of a sphere (centred at the c.o.m. of the host galaxy) that contains the amount of stellar mass equivalent to the mass of the SMBH binary. The sizes of the projected radii were determined through a similar relation to the one described in equation 4.5.

Figures 4.4 and 4.5 show that the core radius estimate depends quite strongly on the used fitting model. However, which of the two models is better for estimating

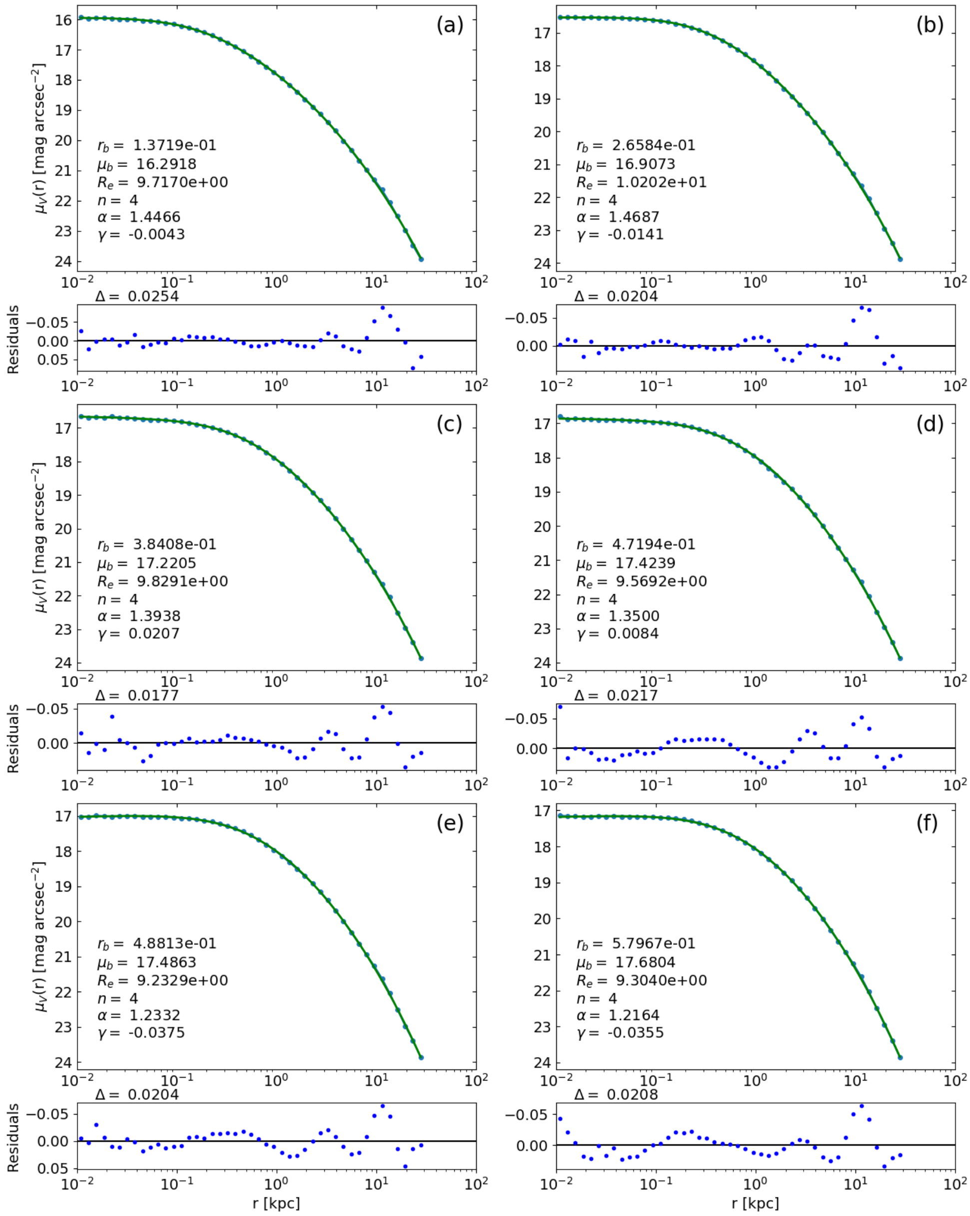

Figure 4.4: Core-Sérsic profile fits of the surface brightness data calculated from all of the individual simulated merger remnants with progenitors containing central supermassive black holes. The letters (a)-(f) denote the different snapshots ((a): BH-1 merger, (b): BH-2 merger, (c): BH-3 merger, (d): BH-4 merger, (e): BH-5 merger, (f): BH-6 merger).

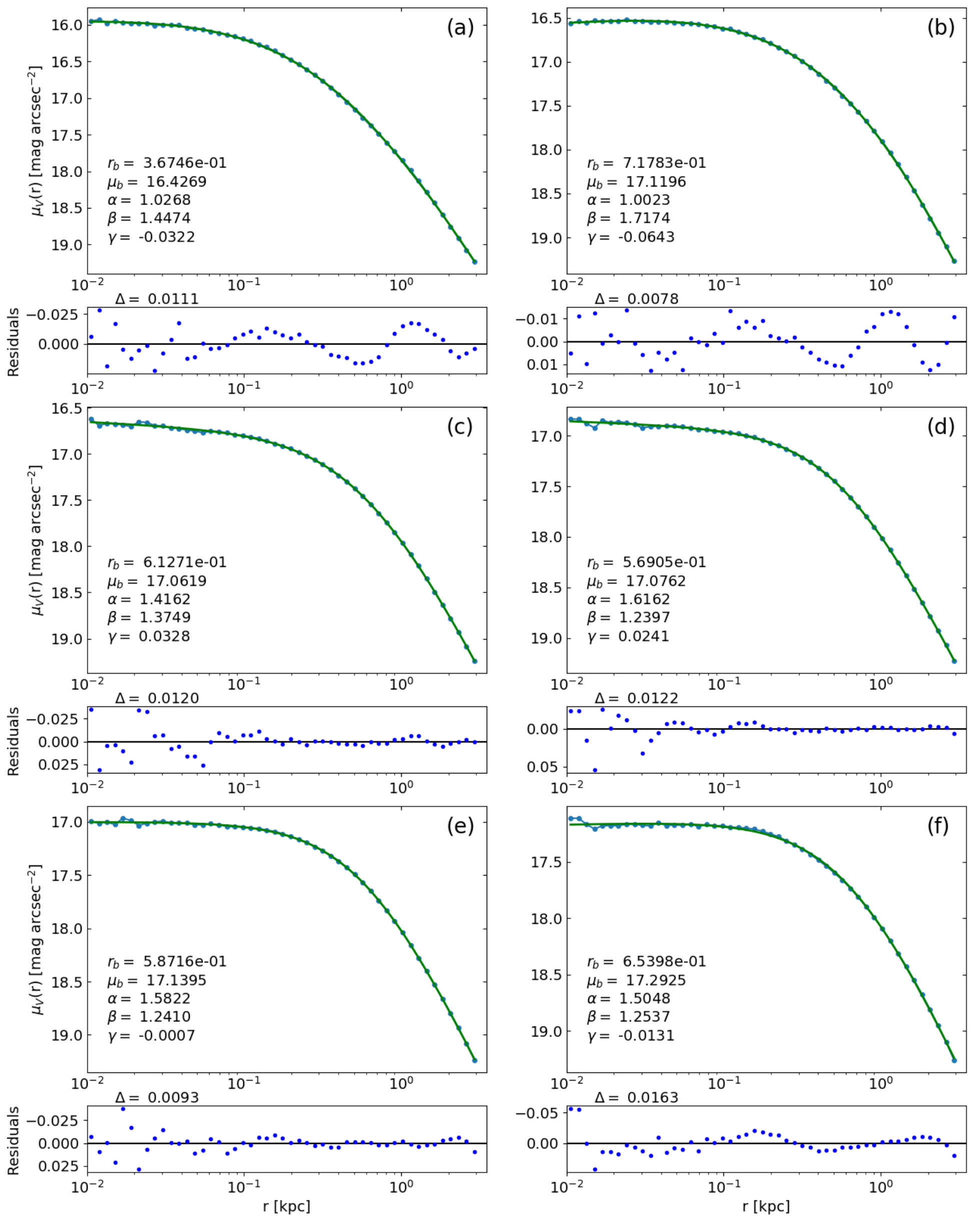

Figure 4.5: Nuker profile fits of the surface brightness data calculated from all of the individual simulated merger remnants with progenitors containing central supermassive black holes. The letters (a)-(f) denote the different merger remnants ((a): BH-1 merger, (b): BH-2 merger, (c): BH-3 merger, (d): BH-4 merger, (e): BH-5 merger, (f): BH-6 merger).

the size of the core is still a matter of debate (Lauer et al., 2007b; Dullo and Graham, 2012). While the RMS of the relative residuals seems to be consistently (although just marginally) smaller for the Nuker model (compare figures 4.4 and 4.5), one also has to take into account that, in the Nuker model, the best-fit value for r_b is strongly dependent on the fitting range (Graham et al., 2003). Furthermore, as stated by Rantala et al. (2018), in order to get sensible values for all of the model parameters (e.g. α, for which $\alpha \lesssim 1$ might even prevent the model from describing the profile as a combination of two power-laws), the fitting range of the Nuker model has to be narrowed down closer to the galactic centre. This, when combined with the parameters' high dependence on the fitting range, shows that the core radius estimations of the Nuker model can be inconsistent.

In addition to the model fitting methods, one could also estimate the size of the core by calculating the so-called "cusp radius" r_γ. The cusp radius is the distance from the centre of the galaxy, at which the logarithmic slope of the surface brightness profile equals $\gamma' = -1/2$ (Carollo et al., 1997; Lauer et al., 2007a). This distance provides an estimate for the location where the inner power-law of the profile changes into the outer power-law, and thus r_γ can be equated to the core radius.

We calculate r_γ for all of the merger remnants with central SMBH binaries (BH-1 - BH-6 mergers) by calculating the gradient of the surface brightness profiles, and then using a function minimization algorithm (Nelder and Mead, 1965) to minimize the difference $\left|\frac{d\mu(r)}{dr} - \left(-\frac{1}{2}\right)\right|$. This allows us to find the radius, at which the gradient gets the value $-1/2$.

Figure 4.6 compares the core radius estimates from each of the three methods for every simulated merger remnant. The break radii from the Nuker fits are consistently larger than the other core radius estimates. They also have, in general, the largest deviations from the other core radii, and even contain two values that seem

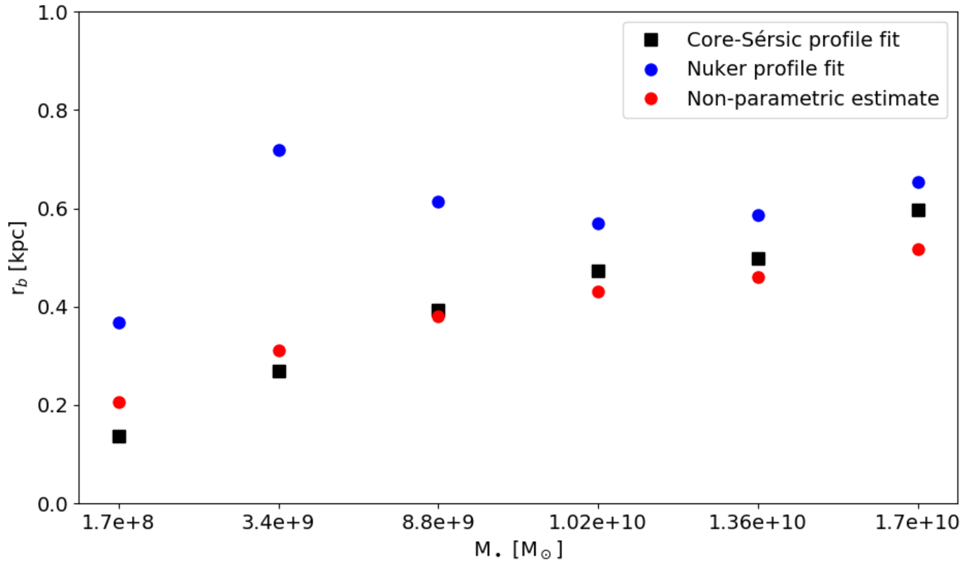

Figure 4.6: Comparison of the different core radius estimates of the merger remnants. These estimates were derived through three different methods: Core-Sérsic profile fitting (black squares), Nuker profile fitting (blue circles) and finding the "cusp radius" (red circles). The x-axis shows the masses of the central SMBH binaries in the merger remnants.

to break the trend of the core radius growing with the central SMBH binary mass (these being the break radii for the BH-2 and BH-3 mergers). Similar larger than expected Nuker core radii can be seen in the analysis of the simulations by Rantala et al. (2018). Similarly to figure 4.6, the difference in their Nuker break radii and the other core radius estimates for the two mergers with the smallest and third smallest central SMBH binaries, are significantly larger than for the other mergers. The fact that these large deviations are present in both our analysis and the analysis by Rantala et al. (2018), further implies that, due to its high dependence on the fitting range, the Nuker model can provide inconsistent values for the break radius. However, when excluding these few Nuker break radii, a clear trend of the size of the core growing with the merger progenitors' central SMBH masses can be seen.

The fact that the size of the core is dependent on the mass of the central SMBH binary is clear evidence towards the cores being formed through a scouring process by the binary black holes. Binaries with larger masses have larger gravitational spheres-of-influence (table 4.2), which naturally leads to the ejection of stellar particles that orbit farther away from the galactic centre (the larger SMBH binary mass also causes the stellar material to be ejected at a larger velocity).

This positive correlation between the core size and the SMBH binary mass has also been identified in independent measurements of the break radius and the central SMBH mass in cored galaxies (e.g. de Ruiter et al., 2005; Lauer et al., 2007a; Thomas et al., 2016). The fact that this effect can be seen, not only in the simulations but also in the observations, makes it clear that merging SMBH binaries are a likely source for the observed cores.

Alongside the size of the core, the surface brightness deficit also becomes larger as the central SMBH binary mass grows, as can clearly be seen in figure 4.2. This can be explained trough the concept of the loss-cone. Binney and Tremaine (2008) show that only stars with the angular momentum:

$$L \lesssim [G(M_1 + M_2)a]^{1/2}, \tag{4.15}$$

where M_1 and M_2 are the masses of the binary black holes, interact strongly enough with the binary to be ejected from the system (i.e. are inside the loss-cone). As the above equation implies, the upper limit of this condition grows alongside the binary mass. This causes more of the orbiting stellar particles to be located in the strong interaction range; as not only does the loss-cone widen, allowing for the ejection of particles with orbits more parallel to the plane of the binary; but the maximum velocities, at which a stellar particle can interact strongly with the binary, also become larger. Thus, a larger SMBH binary mass naturally results in the ejection of a larger number of stellar particles, which then leads to the growth of the central surface brightness deficit.

4.3 Velocity Anisotropy

Another method of studying whether a galaxy has formed a core through core scouring by binary black holes, is to study the velocity anisotropy profile defined in Binney and Tremaine (2008) as:

$$\beta(r) = 1 - \frac{\sigma_\theta^2 + \sigma_\phi^2}{2\sigma_r^2} = 1 - \frac{\sigma_t^2}{\sigma_r^2}, \tag{4.16}$$

where σ_θ, σ_ϕ and σ_r are one-dimensional velocity dispersions in the spherical coordinates, and $\sigma_t = \sqrt{(\sigma_\theta^2 + \sigma_\phi^2)/2}$ is the tangential velocity dispersion. This β-parameter describes the ratio of tangential velocity dispersion in the stellar system to the radial velocity dispersion and, as such, provides information about the nature of the stellar orbits around the black hole binary. A negative value for β shows an abundance of tangential orbits, whereas a positive β corresponds to an abundance of radial orbits.

Figure 4.7 shows β-profiles calculated from all of the final merger remnant snapshots using equation 4.16. In order to get the velocity dispersions, the stellar particles of the remnants were first divided into logarithmic bins, and their velocities were changed from a Cartesian to a spherical coordinate system. Next, the root-mean-squares, which correspond to the velocity dispersions, of the different spherical velocity components were calculated for each bin separately, resulting in a β-value for every bin. Plotting these values gives us the aforementioned profiles in figure 4.7.

According to the β-profiles, the outer areas of the remnants are dominated by radial orbits (positive β), while the majority of orbits near the centre are tangential (negative β). As the initial merger progenitors used in the simulations contained isotropic β-profiles ($\beta = 0$), an area with negative β in the merger remnant would imply that the stars on radial orbits have been lost from the system. It has been shown that hardening black hole binaries can eject stars on highly radial orbits from the galactic core, which results in the central region becoming dominated by mostly

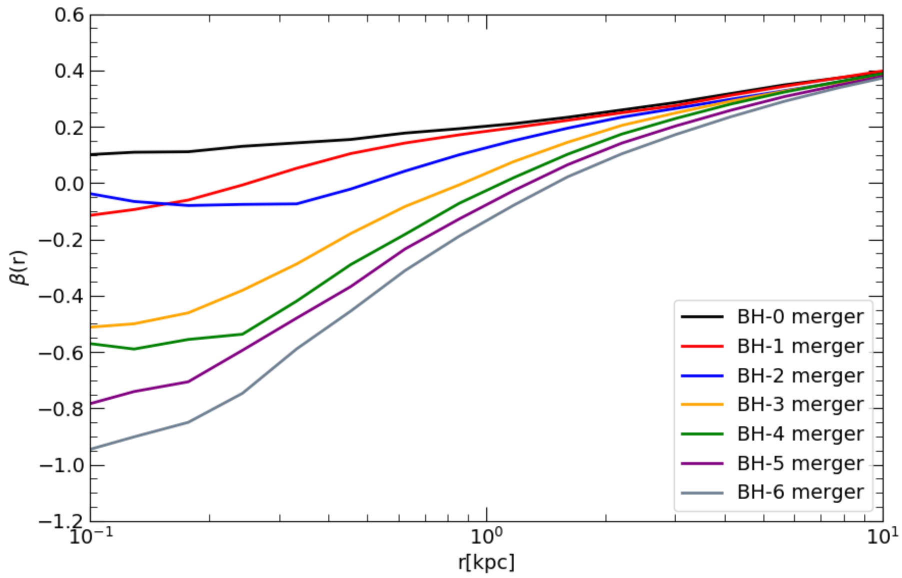

Figure 4.7: Velocity anisotropy (beta) profiles for every simulated merger remnant. The profiles are calculated from the velocity dispersions in radial logarithmic bins, using equation 4.16. Going from the outer regions to the central regions of the merger remnants, the profiles of the remnants with SMBH binaries go from being radially dominated to being tangentially dominated.

tangential orbits (and thus a negative β). The ejected stars can then, in turn, cause the outer orbits to become more radial (Quinlan and Hernquist, 1997; Milosavljević and Merritt, 2001; Thomas et al., 2014).

Figure 4.7 clearly shows that the presence of an SMBH binary has an effect on the shape of the β-profiles. Not only is the slope of the profile steeper for merger remnants which contain a more massive central SMBH binary, but the only merger with a profile that is completely dominated by radial velocity dispersion, is the one without a central SMBH binary (the BH-0 merger).

The shapes of the profiles also make sense in the context of ejection of stellar particles by hardening black hole binaries. The larger the mass of the SMBH binary is, the larger its gravitational sphere-of-influence, which results in more of the radially orbiting stellar particles being ejected.

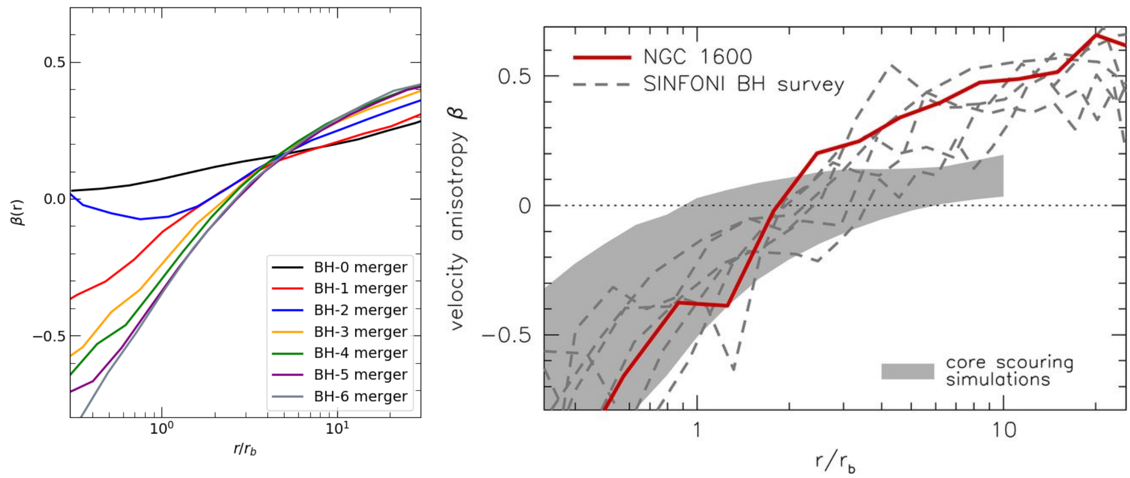

(a) Simulated merger remnants **(b)** NGC 1600

Figure 4.8: (a): The β-profiles of the simulated merger remnants as a function of distance from the centre, scaled by their respective break radius. For the merger remnant without a core (BH-0), the value used for the break radius is $r_b = 1$ kpc. The profile for the BH-2 merger shows an increase in the value of β near the centre of the merger remnant, which is simply the same increase seen in figure 4.7 amplified by the break radius scaling. (b): β-profile of NGC 1600, alongside profiles of galaxies from the SINFONI black hole survey (Saglia et al., 2016) and the range of possible anisotropies found in N-body simulations of the core scouring mechanism (Thomas et al., 2016).

Figure 4.8 shows, both the observed β-profile of NGC 1600 and the profiles from our simulated merger remnants. The profiles in the figure are scaled by the core radius of the respective galaxy. Even by eye, it can clearly be seen that the β-profiles from both the simulations and the observations of NGC 1600 are similar to each other (not counting the anomalous profile for the BH-2 merger). However, looking closely at the values on the axes of the plots, the observed profile of NGC 1600 seems to be somewhat steeper when compared to any of the simulated ones.

According to Rantala et al. (2018), the kinematics being more tangential close to the core in NGC 1600 than in the simulations, could be caused by further adiabatic growth of the merged central SMBH's mass. Young (1980) shows that black holes that grow adiabatically through, for example accretion of gas, can cause the surrounding stellar orbits to become more tangential. If the time scale of the mass growth is smaller than the relaxation time scale of the galaxy while also being larger than the dynamical time scale of the stellar system, the growth can be considered adiabatic. This results in the conservation of the angular momentum and the radial action of the stellar orbits (radial action being one of the momenta in the canonical Hamiltonian coordinates called *angle-action variables* (e.g. Binney and Tremaine, 2008), which, due to the now higher gravitational potential induced by the central black hole, causes the orbits to become more circular. Although this effect is not strong enough to account for the entire shape of the β-profile (Thomas et al., 2016), it could certainly be a reason for the more tangentially dominated core regions seen in the observations.

As for the outer region of the β-profile of NGC 1600, it is possible, that the reason why it is more radially dominated than any of the outer parts in the simulated merger remnants, is due to the lack of minor-mergers in the simulations (Rantala et al., 2018). These minor-mergers would deposit all of their mass in the outer regions of the galaxy, and would thus disrupt only the outer stellar orbits, making some of the more tangential of these orbits more radial. Furthermore, they would not contribute to the destruction of radial orbits near the centre of the galaxy, as the smaller progenitor galaxy would not contain a central SMBH.

4.4 Line-of-Sight Kinematics

4.4.1 2D Kinematic Maps

In order to make sure that the KETJU simulations produce results which are in agreement with observations, I also analyse the line-of-sight (LOS) kinematics of the simulated merger remnants. The analysis is focused on four different LOS velocity distribution parameters: the average LOS velocity V_{avg}, the velocity dispersion σ, and the h_3 and h_4 parameters which correspond to the skewness and the kurtosis of the distribution respectively. The distribution from which these properties are calculated is defined as the following modified Gaussian function (van der Marel and Franx, 1993; Bender et al., 1994):

$$f(v) = I_0 e^{-\gamma^2/2}(1 + h_3 H_3(y) + h_4 H_4(y)), \tag{4.17}$$

where I_0 is a normalization constant, γ is the central slope of the particle density profile, $y = (v - V_{\mathrm{avg}})/\sigma$, and H_3 and H_4 are the third and fourth order Hermite polynomials respectively:

$$H_3(y) = \left(2\sqrt{2}y^3 - 3\sqrt{2}y\right)/\sqrt{6}, \tag{4.18}$$

$$H_4(y) = \left(4y^4 - 12y^2 + 3\right)/\sqrt{24}. \tag{4.19}$$

The above properties are calculated using a Python-script (Matteo Frigo, internal communication), which makes use of the Voronoi tessellation algorithm by (Cappellari and Copin, 2003) in order to provide binned statistics of the LOS velocities. First, when using the script, the "line-of-sight" is defined as the intermediate axis of the merger remnant, after which the remnant is oriented accordingly using the inertia tensor. The 2D line-of-sight projection of the remnant is then divided into "spaxels" (or simply bins) using the aforementioned Voronoi tessellation algorithm. The shape and size of the spaxels are determined so that each one contains the same signal-to-noise ratio, which in our simulated case is defined as the number of stellar particles. The LOS-velocities inside the spaxels are then made into a histogram, into which the modified Gaussian function described in equation 2.13 is fitted. This gives the values of the LOS-velocity distribution parameters: V_{avg}, σ, h_3 and h_4 for the spaxel in question. Finally, the values of the spaxels can be plotted, resulting in 2D voronoi binned maps of all of the four parameters.

Figure 4.9 shows the voronoi binned 2D maps of the four LOS velocity distribution parameters for the simulated BH-0 merger (no central SMBH) and the BH-6 merger (largest central SMBH), as well as for two observed galaxies NGC 3414 and NGC 4111. The contours, which are added to help visualise the shape of the galaxy, denote flux isophotes of the merger remnants, and have a spacing of one magnitude. Similar maps for the rest of the simulated merger remnants can be seen in figure 4.10. Figure 4.10 shows the IFU-maps of the four LOS-velocity parameters for the rest of the simulated merger remnants.

The IFU maps in figures 4.9 and 4.10 show that the average LOS velocities of the simulated merger remnants are far from isotropic, with most of the remnants containing central binary SMBHs showcasing counter-rotating central regions also known as "kinematically decoupled cores" (KDC). Some of the simulated remnants (BH-4 - BH-6 mergers) even contain another counter rotating structure inside the KDC (Rantala et al., 2019). These features, alongside the relatively low average LOS-velocities, are often found in galaxies called "slow rotators" (Emsellem et al., 2007). Slow rotator galaxies are early-type galaxies which are assumed to have been formed through gas-poor "dry" mergers (Emsellem et al., 2007; Cappellari et al., 2007); processes not unlike the ones simulated in our simulations. As such, the merger remnants being slow rotators is a somewhat expected result.

Figures 4.9 and 4.10 also contain IFU-maps of the velocity dispersion in the simulated merger remnants. These maps show a clear connection between the mass of the central SMBH binary and the velocity dispersion at the centre of the galaxy. The presence of an SMBH binary causes the formation of a central velocity dispersion peak in the σ-distribution, the strength of which correlates positively with the mass of the binary. Furthermore, as the mass of the SMBH binary grows, the size of the area with the highest velocity dispersion in the galaxy also grows. Additionally, the growing binary mass seems to cause the high-σ area to get more and more aligned with the major-axis of the galaxy. Most of these effects can easily be identified when comparing the IFU-maps of the different simulated merger remnants from figure 4.10. The formation of the velocity dispersion peak, which is simply caused by the presence of the SMBH binary, is demonstrated in the IFU-maps of the BH-0 and BH-6 merger remnants in figure 4.9. The positive correlation between the mass of the central SMBH (or in the case of the simulations: central SMBH binary) and the velocity dispersion of its host galaxy has been observed in a multitude of galaxies with central SMBHs, both cored and non-cored (Ferrarese and Merritt, 2000).

Apart from the BH-0 merger remnant, the h_3-parameter values in the IFU-maps of the simulated merger remnants show an anti-correlation with the average LOS-velocity. Indeed, Krajnović et al. (2011) have found that, while the anti-correlation between the LOS velocities and the h_3-parameter is mostly found in fast rotators (see central region of NGC 4111 in figure 4.9), some galaxies with counter-rotating cores (CRC) also exhibit this behaviour. This anti-correlation can be seen in NGC 3414 from figure 4.9. Once again, the simulated KETJU results agree with the observations.

The h_4-parameter roughly corresponds to the velocity anisotropy parameter

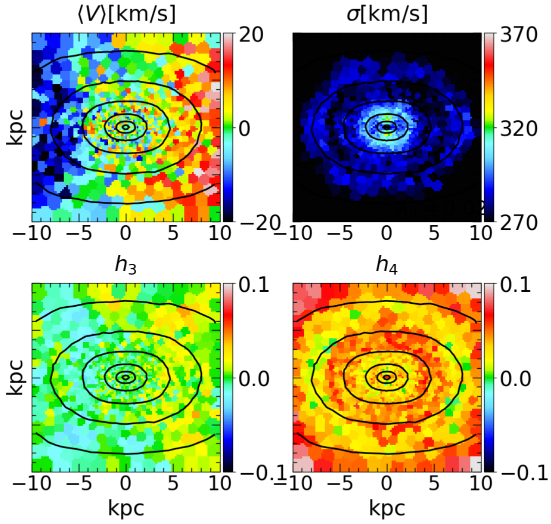

(a) BH-0 merger remnant

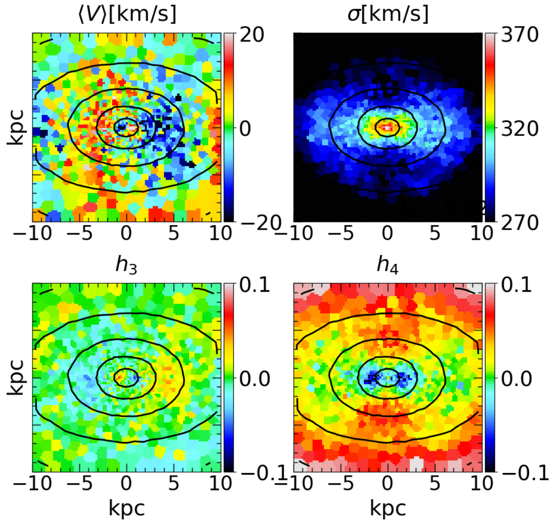

(b) BH-6 merger remnant

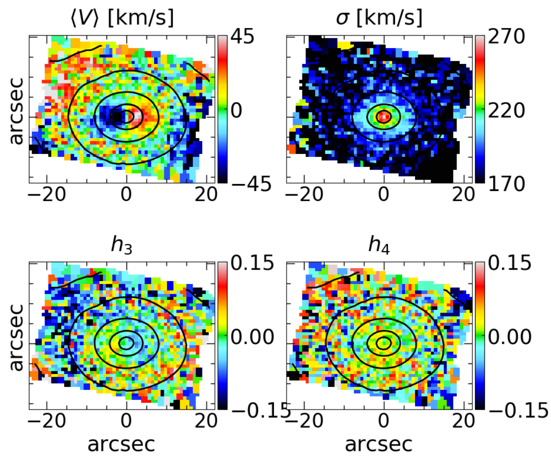

(c) NGC 3414

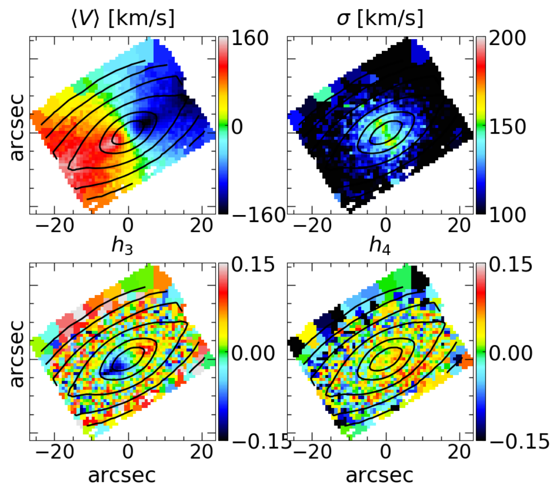

(d) NGC 4111

Figure 4.9: IFU-maps of average LOS-velocities, velocity dispersion, h_3 parameters and h_4 parameters from two simulated merger remnants and two observed galaxies. The four maps in figure (a) are from the BH-0 merger, and the four in figure (b) are the BH-6 merger. Figures (c) and (d) show IFU-maps of known slow (NGC 3414) and fast rotator (NGC 4111) galaxies from the ATLAS^{3D} survey (Emsellem et al., 2004; Cappellari et al., 2011; Krajnović et al., 2011).

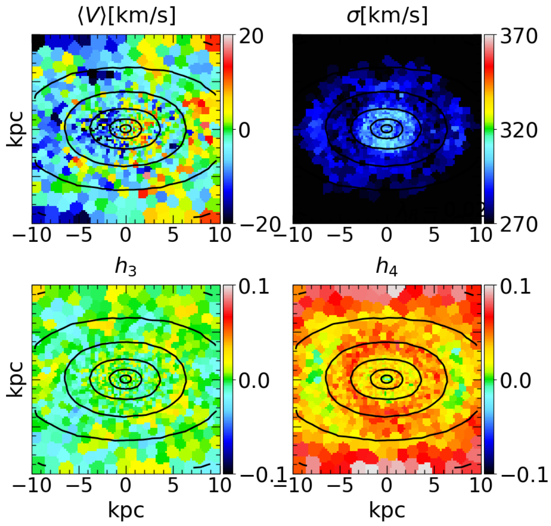

(a) BH-1 merger

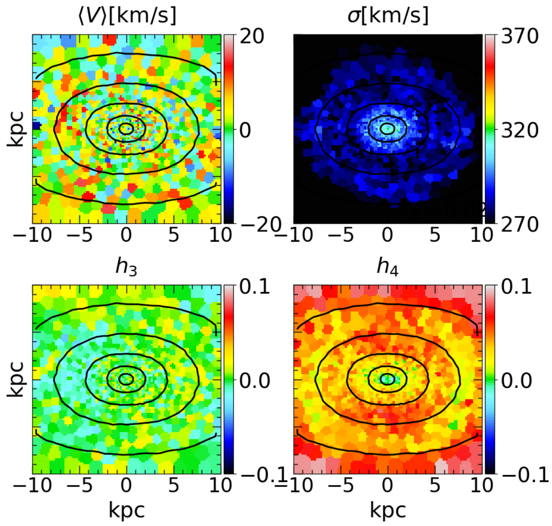

(b) BH-2 merger

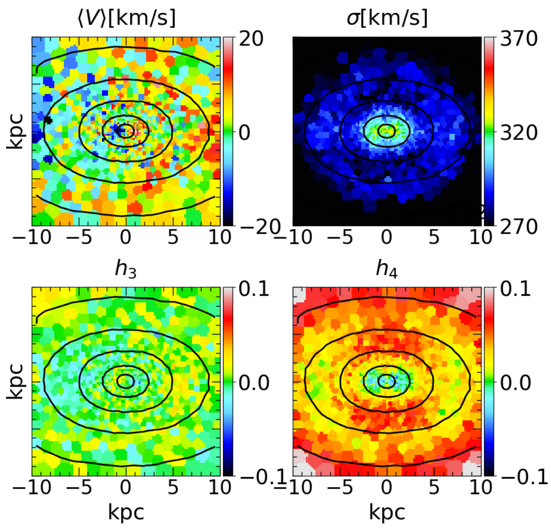

(c) BH-3 merger

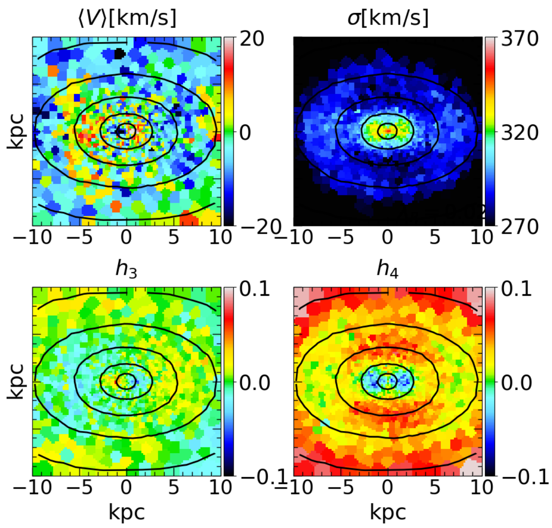

(d) BH-4 merger

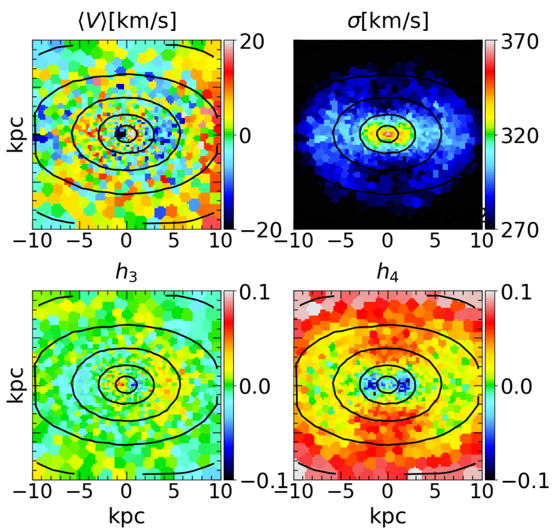

(e) BH-5 merger

Figure 4.10: IFU-maps of average LOS-velocities, velocity dispersion, h_3 parameters and h_4 parameters from four simulated merger remnants: BH-1, BH-2, BH-3, BH-4 and BH-5 mergers.

β, where a negative value of h_4 identifies areas with a large tangential velocity dispersion, and a positive identifies areas with a more radial velocity dispersion (Gerhard, 1993; Gerhard et al., 1998; Thomas et al., 2007). Comparing the β-profiles from figure 4.7 with the h_4 IFU-maps from figures 4.9 and 4.10, this certainly seems to be the case. For the merger remnants with central SMBH binaries, both the β and the h_4 values are largely positive in the outer regions of the galaxy, while being negative closer to their centres. The h_4 map of the BH-0 merger is then positive all around, exactly like its β-profile. The h_4 maps of NGC 3414 and NGC 4111 (figure 4.9) do not contain any specific structures and seem to be completely isotropic. As the negative h_4-areas in the IFU maps of the simulated merger remnants are likely caused by core scouring, and as neither of the observed galaxies are cored galaxies (Lauer et al., 2007b); they most likely have not experienced such a process, making the lack of clear structures understandable.

4.4.2 The λ_R-parameter

Further analysis of the kinematics of the simulated merger remnants can be done by studying the λ_R parameter, which describes the angular momentum of a galaxy (Emsellem et al., 2007). More importantly, the parameter allows us to differentiate between the aforementioned slowly rotating galaxies and so-called fast rotators (see figure 4.9) (Emsellem et al., 2007). The parameter itself is defined in a general form as:

$$\lambda_R \equiv \frac{\langle R|V|\rangle}{\langle R\sqrt{V^2+\sigma^2}\rangle}, \tag{4.20}$$

where R is the projected distance from the galactic centre, V is the line-of-sight velocity, σ is the velocity dispersion and $\langle\ \rangle$ denote that the nominator and denominator in the equation are luminosity weighted means. However, as most of the observational kinematic analysis of galaxies is done through binned 2D spectroscopy, and as the IFU-maps made from our simulations are produced the same way as the observed ones, we will be using the following version of the equation:

$$\lambda_R = \frac{\sum_{i=1}^{N_p} F_i R_i |V_i|}{\sum_{i=1}^{N_p} F_i R_i \sqrt{V_i^2 + \sigma_i^2}}, \tag{4.21}$$

where F_i, R_i, V_i and σ_i are the flux, projected distance from the galaxy centre, velocity and velocity dispersion of the ith bin, and N_p is the number of bins. In the case of our simulations, the N_p bins used are of course the voronoi bins described earlier in this section.

Determining whether a galaxy is either a fast or a slow rotator using λ_R, is done by comparing the value that the parameter gets at the galaxy's effective radius, to some pre-defined threshold. The originally used threshold is: $\lambda_{Re} < 0.1$, where λ_{Re} is the aforementioned λ_R at the effective radius, and where galaxies fulfilling this condition are classified as slow rotators (Emsellem et al., 2007). A revision of the threshold by Emsellem et al. (2011) takes the ellipticity (ϵ) of the galaxy into account, and defines slow rotators as having $\lambda_{R_e} < 0.31\sqrt{\epsilon}$, which accounts for the increased anisotropy in the kinematics of flatter galaxies. An even further refinement of the slow rotator definition has been proposed by Cappellari (2016), where slow rotator galaxies are determined using the following two criteria: $\lambda_{R_e} < 0.08 + \epsilon/4$ and $\epsilon < 0.4$. The former criterion of the threshold reduces the risk of misidentifying very round non-regular slow rotators as fast rotators, while the latter makes sure that only sufficiently round galaxies are classified as slow rotators (Cappellari 2016 argues that "genuine" disk-less slow rotators are all rounder than $\epsilon = 0.4$).

As two of the three aforementioned slow rotator thresholds require us to know the ellipticity of the galaxy I wrote a program in Python that calculates ellipticities of the simulated merger remnants. These ellipticity calculations are done using a method described in Zemp et al. (2011), which uses the shape tensor:

$$\mathbf{S} = \frac{\int_V \rho(\mathbf{r})\omega(\mathbf{r})\mathbf{r}\mathbf{r}^T \, dV}{\int_V \rho\mathbf{r} \, dV}, \tag{4.22}$$

where $\mathbf{r}$ is position from the galactic centre, $\rho(\mathbf{r})$ is the mass density, V is the volume of an enclosed ellipsoid with the elliptical radius r_{ell}, and where the weighting function $\omega(\mathbf{r}) = 1$. The eigenvalues of the shape tensor correspond to $a^2/3$, $b^2/3$ and $c^2/3$; where a, b and c are the semi-principal axes; and they can be used to calculate the ellipticity as $\epsilon = 1 - b/a$.

However, simply calculating the shape tensor and getting the correct eigenvalues is not possible, as the elliptical radius r_{ell} is defined, in part, by using the axis ratios a/b and a/c:

$$r_{\text{ell}} = \sqrt{x_{\text{ell}}^2 + \frac{y_{\text{ell}}^2}{(b/a)^2} + \frac{z_{\text{ell}}^2}{(c/a)^2}}. \tag{4.23}$$

This means that we have to turn the calculation into an iterative process by starting with $b/a = c/a = 1$ for the initial value of r_{ell}, and calculating new shape tensor eigenvalues using previously gained axis ratios until the values of the ratios start to converge.

We calculate λ_{Re} and ϵ_e, i.e. the ellipticity at the effective radius (the ellipticity is calculated using $r_{\text{ell}} = R_e$, and a convergence criterion of a difference smaller than 10^{-3} between consequent axis ratios), for every merger simulation snapshot and plot them against each other. We also plot the previously mentioned slow rotator thresholds, as well as observations from the ATLAS^{3D}-survey (Cappellari et al., 2011), in the same figure. The resulting plot can be seen in figure 4.11.

Regardless of the threshold used for differentiating between slow and fast rotators, figure 4.11 shows us that, all of the simulated merger remnants are clearly classified as slow rotators. This agrees well with the kinematic anisotropies seen in the IFU maps, which also implied a slow rotator classification for the remnants.

4.5 Comparison to Observations

As the physical properties of the merger progenitors are modelled after NGC 1600, it is interesting to see how the results from the simulations compare with actual

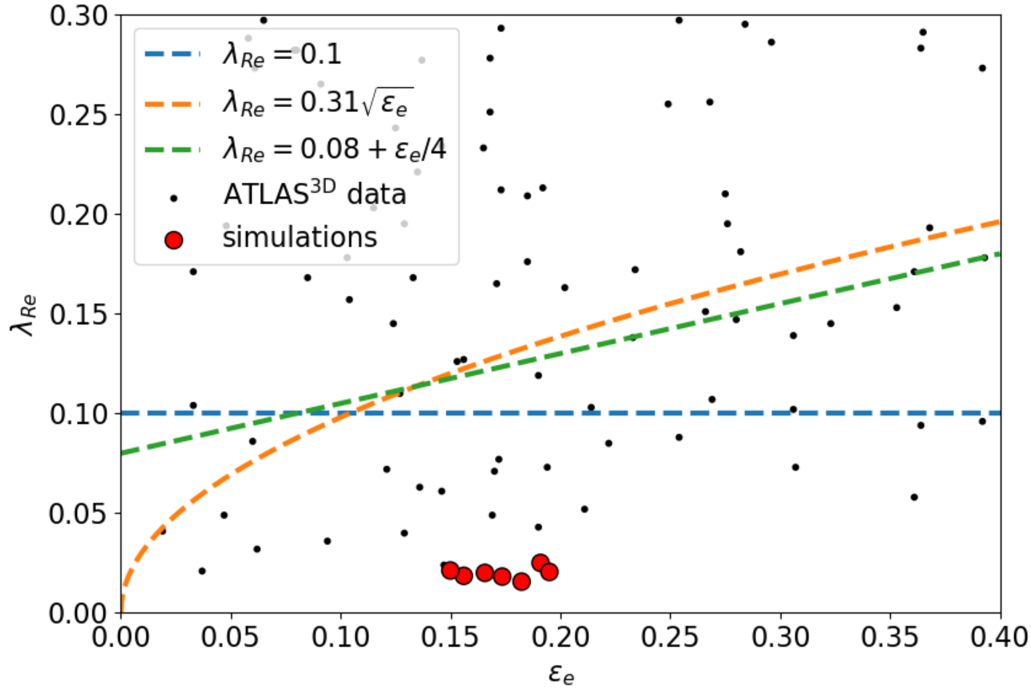

Figure 4.11: Values of the λ_{Re}-parameter of galaxies, plotted against their ellipticity at the effective radius. The red dots correspond to the simulated merger remnants, whereas the black dots correspond to galaxies observed in the ATLAS^{3D}-survey (Cappellari et al., 2011; Emsellem et al., 2011). The dashed lines display different slow rotator thresholds as a function of ellipticity (Emsellem et al., 2007, 2011; Cappellari, 2016).

observations of the galaxy. While I will be comparing the observations mainly to the BH-6 merger remnant, as the mass of the SMBH binary in the simulated galaxy is equivalent to the observed and modelled mass of the central SMBH in NGC 1600 ($M_\bullet = 1.7 \times 10^{10} M_\odot$) (Thomas et al., 2016); I will also be comparing the observed properties of the cored massive elliptical galaxy NGC 4472 to the simulated BH-1 merger remnant. Both of the latter galaxies have similar central black hole masses (or in the case of the simulated remnant, black hole binary mass), as well as similar total stellar masses. Thus, comparing their other physical properties could provide some interesting insight into the formation of cores.

Figure 4.12 shows core-Sérsic profile fits of the surface brightness profiles from

	BH-1 merger	NGC 4472	BH-6 merger	NGC 1600
r_b [kpc]	0.137	0.151	0.579	0.667
μ_b [mag arcsec^{-2}]	16.29	16.48	17.68	18.00
R_e [kpc]	9.717	16	9.304	16.04
n	4	5.6	4	5.83
α	1.45	3.05	1.22	2.09
γ	0.00	0.06	−0.04	0.03

Table 4.3: Best-fit parameters of the core-Sérsic profile fits seen in figure 4.12. The best-fit parameters of NGC 4472 are from Rusli et al. (2013a), while the parameters for NGC 1600 are given in Thomas et al. (2016). n is the Sérsic index, α controls the sharpness of the transition between the inner and outer profiles, and γ is the slope of the inner profile.

the BH-1 and BH-6 mergers, and compares them to the profile fits from the observed core galaxies NGC 4472 and NGC 1600 respectively. Not only do the shapes of the compared photometric profiles follow each other closely in both cases, the best-fit parameters are also quite closely related (table 4.3).

Another comparison between some of the properties of the four galaxies can be seen in table 4.4. Most importantly, the table shows that the kinematic properties of the simulated merger remnants and the kinematic properties of NGC 1600 are very similar. On the other hand, compared to the three other galaxies, the spin parameter and line-of-sight velocity of NGC 4472 are almost an order of magnitude larger. Furthermore, like the simulated galaxies, NGC 1600 can easily be identified as a slow rotator by its λ_e parameter and ellipticity, while NGC 4472 seems to be classified as a fast rotator.

Before drawing conclusion from these results, it is important to know that, whether NGC 4472 is in fact classified as a fast rotator is not known for certain. Emsellem et al. (2011) found a significantly lower value for its spin parameter ($\lambda_e = 0.077$), which would easily classify the object as a slow rotator. The value used in this analysis comes from the more recent MASSIVE-survey (Ma et al., 2014; Veale et al., 2017), in which some of the inaccuracies of the previous observations were shown (e.g. not taking into account a large enough region of the observed galaxy). Conceding to some possible biases in their own calculations, Veale et al. (2017) ultimately classify NGC 4472 as an intermediate case between slow and fast rotators.

It is impressive, that the simulation of the BH-6 merger is able to reproduce both the kinematic properties and the shape of the surface brightness profile of NGC 1600 so well. Since the simulation describes a dry major merger event between two massive ETG with central SMBHs, the results imply that this process could be the formation mechanism behind core galaxies.

Interestingly, since the BH-6 merger has extremely similar kinematic properties with the BH-1 merger and NGC 1600, it can be assumed that the mass of the central SMBH binary does not affect the rotation of its host galaxy in any significant way. This suggests that, as far as the merger progenitors are concerned, it is the properties other than their central SMBH mass (i.e. them being massive gas-poor ETGs) that determine the stellar kinematics in the final merger remnant. As for NGC 4472, since both its λ_e and LOS velocity are about an order of magnitude larger compared to the three other galaxies, it can be argued that its formation history must be quite different when compare to the other galaxies. However, due to the ambiguity of whether NGC 4472 is a fast rotator and whether its spin parameter is biased towards large values, the possibility that the galaxy has also formed through a dry ETG merger, should not be ruled out.

Earlier in this chapter it was shown that there is a clear positive correlation between the central SMBH binary masses and the size of the core radii. However, the fact that the core radius sizes for the BH-1 merger remnant and NGC 4472 are comparable, and that many of their other properties are quite different; imply that, not only is there a correlation, the SMBH binary mass might be the only property that affects the size of the core in any significant way. If this is true, it is very strong

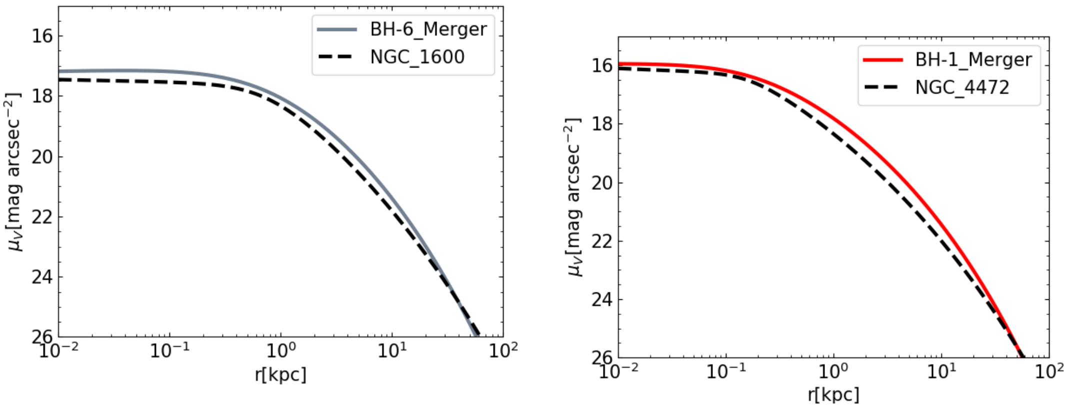

Figure 4.12: Comparison between core-Sérsic profile fits from observed galaxies and simulated merger remnants, where the surface brightness is given in V-band magnitudes. The figure on the left compares the profile of the BH-6 merger remnant (the merger remnant whose progenitors containing the largest central SMBH masses) to NGC 1600; while the figure on the right compares the profiles of the BH-1 merger remnant (the remnant with progenitors that had the smallest SMBH masses) and NGC 4472. The parameters for plotting the core-Sérsic profile of NGC 1600 were taken from Thomas et al. (2016), with the units being changed to the above, by assuming $V - R = 0.5$ (the same assumption being done in Lauer et al. (2007b)), and by using the distance $D = 64$Mpc (Thomas et al., 2016) to define the relation between arc seconds and parsecs. The parameters for the profile of NGC 4472 were from Rusli et al. (2013a). All of the best-fit parameters can be found in table 4.3

evidence, that the cores are formed through a scouring process by binary SMBHs.

Galaxy	$M_\star$	$M_\bullet$	R_e	μ_e	n	$V_{\rm LOS}$	σ_e	λ_e	ϵ_e
	$[\times 10^{11} M_\odot]$	$[\times 10^{10} M_\odot]$	[kpc]	[mag/arcsec^2]		[km/s]	[km/s]		
(1)	(2)	(3)	(4)	(5)	(6)	(7)	(8)	(9)	(10)
BH-6 merger	8.3	1.7	10.722	21.54	4	5.61	278	0.0213	0.15
NGC 1600	8.3	1.7	~ 16	~ 22.8	5.83	7.1	293	0.026	0.32
BH-1 merger	8.3	0.17	9.879	21.42	4	5.49	274	0.021	0.195
NGC 4472	6.03	0.25	14.33	22.72	5.6	45.4	258	0.197	0.172

Table 4.4: Comparisons between the physical properties of the simulated BH-1 and BH-6 merger remnants and the observed galaxies NGC 1600 and NGC 4472 respectively. The properties described in the columns are explained below, alongside the sources for their values in NGC 1600 and NGC 4472.

(1) Name of the galaxy.

(2) Total stellar mass. NGC 1600: Thomas et al. (2016), NGC 4472: Veale et al. (2018).

(3) Central SMBH / central SMBH binary mass. NGC 1600: Thomas et al. (2016), NGC 4472: Rusli et al. (2013b).

(4) Effective radius. The values used for the simulated mergers are estimated by calculating the half-mass radius in three dimensions, and using equation 4.5 to get the approximate two dimensional effective radius. This is done instead of using the core-Sérsic profile best-fit parameter, since the core-Sérsic R_e only takes into account the specific fitting radius. NGC 1600: Thomas et al. (2016), where the value is changed from arc seconds to kpc by assuming that the galaxy is located at the distance of $D = 64$ Mpc; NGC 4472: Veale et al. (2017).

(5) Surface brightness at the effective radius. The values for all of the galaxies are calculated from the core-Sérsic fits. The profile fits best-fit parameters are from table 4.3.

(6) Sérsic index. NGC 1600: Thomas et al. (2016), NGC 4472: Rusli et al. (2013a).

(7) Mean line-of-sight velocity inside the effective radius. For the the simulated mergers these values are calculated from their respective IFU maps as the mean of the V_{LOS}-values from the Voronoi-bins inside the effective radius. NGC 1600 and NGC 4472: Bender et al. (1994).

(8) Velocity dispersion inside the effective radius. As with V_{LOS}, this value comes from the mean velocity dispersion of the Voronoi bins inside the effective radius in the IFU-maps for the simulated mergers. NGC 1600 and NGC 4472: Veale et al. (2017).

(9) Spin parameter at the effective radius. NGC 1600 and NGC 4472: (Veale et al., 2018).

(10) For the simulated mergers and NGC 4472: ellipticity of the galaxy at the effective radius. For NGC 1600: luminosity weighted ellipticity. NGC 1600: Goullaud et al. (2018), NGC 4472: Emsellem et al. (2011).

5. Conclusions

A. Figures

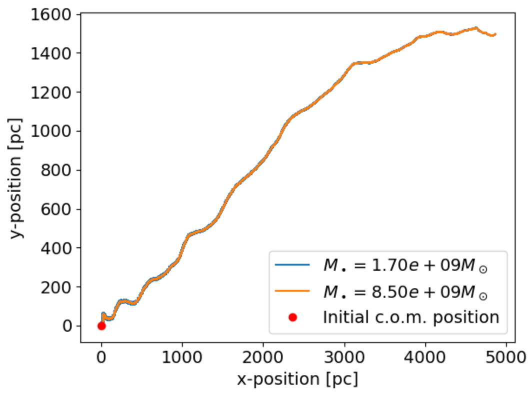

(a) Run 1

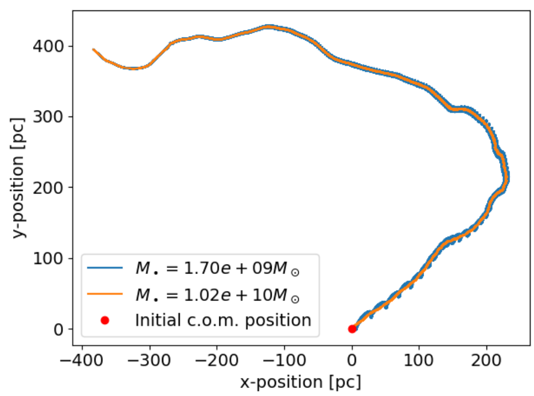

(b) Run 2

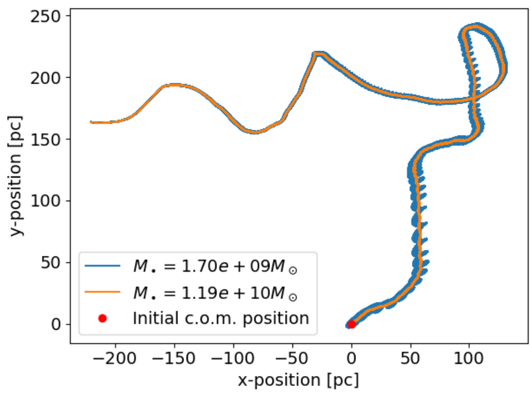

(c) Run 3

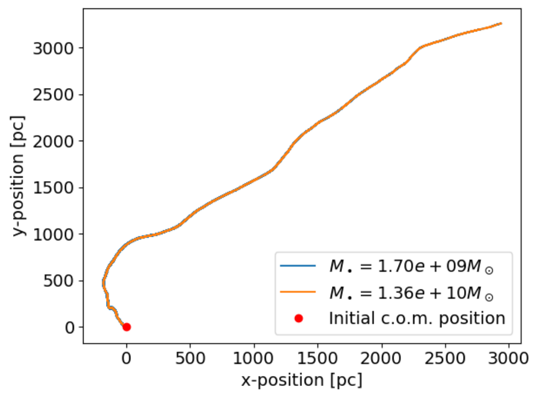

(d) Run 4

Figure A.1: The trajectories of the black holes from simulation runs by Mannerkoski et al. (2019). The coordinates are centred on the initial location of the centre-of-mass of the black hole system. The orange and blue lines show the paths taken by the smaller and larger black holes respectively during the simulation.

Bibliography

B. P. Abbott et al. Observation of Gravitational Waves from a Binary Black Hole Merger. *Physical Review Letters*, 116(6):061102, Feb 2016. doi: 10.1103/PhysRevLett.116.061102.

B. P. Abbott et al. GWTC-1: A Gravitational-Wave Transient Catalog of Compact Binary Mergers Observed by LIGO and Virgo during the First and Second Observing Runs. *Physical Review X*, 9(3):031040, Jul 2019. doi: 10.1103/PhysRevX.9.031040.

R. Bacon, Y. Copin, G. Monnet, Bryan W. Miller, J. R. Allington-Smith, M. Bureau, C. M. Carollo, Roger L. Davies, Eric Emsellem, Harald Kuntschner, Reynier F. Peletier, E. K. Verolme, and P. Tim de Zeeuw. The SAURON project - I. The panoramic integral-field spectrograph. *Monthly Notices of the Royal Astronomical Society*, 326(1):23–35, Sep 2001. doi: 10.1046/j.1365-8711.2001.04612.x.

Joshua E. Barnes and Lars Hernquist. Transformations of Galaxies. II. Gasdynamics in Merging Disk Galaxies. *The Astrophysical Journal*, 471:115, Nov 1996. doi: 10.1086/177957.

Joshua E. Barnes and Lars E. Hernquist. Fueling Starburst Galaxies with Gas-rich Mergers. *The Astrophysical Journal Letters*, 370:L65, Apr 1991. doi: 10.1086/185978.

R. Bender, R. P. Saglia, and O. E. Gerhard. Line-of-sight velocity distributions of elliptical galaxies. *Monthly Notices of the Royal Astronomical Society*, 269: 785–813, Aug 1994. doi: 10.1093/mnras/269.3.785.

James Binney and Scott Tremaine. *Galactic Dynamics: Second Edition*. 2008.

M. Cappellari, E. Emsellem, D. Krajnović, R. M. McDermid, N. Scott, G. A. Verdoes Kleijn, L. M. Young, K. Alatalo, R. Bacon, L. Blitz, M. Bois, F. Bournaud, M. Bureau, R. L. Davies, T. A. Davis, P. T. de Zeeuw, P.-A. Duc, S. Khochfar, H. Kuntschner, P.-Y. Lablanche, R. Morganti, T. Naab, T. Oosterloo, M. Sarzi, P. Serra, and A.-M. Weijmans. The ATLAS^{3D} project - I. A volume-limited sample of 260 nearby early-type galaxies: science goals and selection criteria. *Monthly Notices of the Royal Astronomical Society*, 413:813–836, May 2011. doi: 10.1111/j.1365-2966.2010.18174.x.

Michele Cappellari. Structure and Kinematics of Early-Type Galaxies from Integral Field Spectroscopy. *Annual Review of Astronomy and Astrophysics*, 54:597–665, Sep 2016. doi: 10.1146/annurev-astro-082214-122432.

Michele Cappellari and Yannick Copin. Adaptive spatial binning of integral-field spectroscopic data using Voronoi tessellations. *Monthly Notices of the Royal Astronomical Society*, 342(2):345–354, Jun 2003. doi: 10.1046/j.1365-8711.2003.06541.x.

Michele Cappellari, Eric Emsellem, R. Bacon, M. Bureau, Roger L. Davies, P. T. de Zeeuw, Jesús Falcón-Barroso, Davor Krajnović, Harald Kuntschner, Richard M. McDermid, Reynier F. Peletier, Marc Sarzi, Remco C. E. van den Bosch, and Glenn van de Ven. The SAURON project - X. The orbital anisotropy of elliptical and lenticular galaxies: revisiting the (V/σ, $\in$) diagram with integral-field stellar kinematics. *Monthly Notices of the Royal Astronomical Society*, 379(2):418–444, Aug 2007. doi: 10.1111/j.1365-2966.2007.11963.x.

C. Marcella Carollo, Marijn Franx, Garth D. Illingworth, and Duncan A. Forbes. Ellipticals with Kinematically Distinct Cores: V - I Color Images with WPFC2. *The Astrophysical Journal*, 481(2):710–734, May 1997. doi: 10.1086/304060.

S. Chandrasekhar. Dynamical Friction. I. General Considerations: the Coefficient of Dynamical Friction. *The Astrophysical Journal*, 97:255, Mar 1943. doi: 10.1086/144517.

R. L. Davies, G. Efstathiou, S. M. Fall, G. Illingworth, and P. L. Schechter. The kinematic properties of faint elliptical galaxies. *The Astrophysical Journal*, 266: 41–57, Mar 1983. doi: 10.1086/160757.

H. R. de Ruiter, P. Parma, A. Capetti, R. Fanti, R. Morganti, and L. Santantonio. Are radio galaxies and quiescent galaxies different? Results from the analysis of HST brightness profiles. *Astronomy and Astrophysics*, 439(2):487–496, Aug 2005. doi: 10.1051/0004-6361:20042529.

Gerard de Vaucouleurs. Recherches sur les Nebuleuses Extragalactiques. *Annales d'Astrophysique*, 11:247, Jan 1948.

W. Dehnen. A Family of Potential-Density Pairs for Spherical Galaxies and Bulges. *Monthly Notices of the Royal Astronomical Society*, 265:250, Nov 1993. doi: 10.1093/mnras/265.1.250.

Bililign T. Dullo and Alister W. Graham. Sizing up Partially Depleted Galaxy Cores. *The Astrophysical Journal*, 755(2):163, August 2012. doi: 10.1088/0004-637X/755/2/163.

Bililign T. Dullo and Alister W. Graham. Depleted cores, multicomponent fits, and structural parameter relations for luminous early-type galaxies. *Monthly Notices of the Royal Astronomical Society*, 444(3):2700–2722, Nov 2014. doi: 10.1093/mnras/stu1590.

E. Emsellem, M. Cappellari, R. F. Peletier, R. M. McDermid, R. Bacon, M. Bureau, Y. Copin, R. L. Davies, D. Krajnović, H. Kuntschner, B. W. Miller, and P. T. de Zeeuw. The SAURON project - III. Integral-field absorption-line kinematics of 48 elliptical and lenticular galaxies. *Monthly Notices of the Royal Astronomical Society*, 352:721–743, August 2004. doi: 10.1111/j.1365-2966.2004.07948.x.

E. Emsellem, M. Cappellari, D. Krajnović, K. Alatalo, L. Blitz, M. Bois, F. Bournaud, M. Bureau, R. L. Davies, T. A. Davis, P. T. de Zeeuw, S. Khochfar, H. Kuntschner, P.-Y. Lablanche, R. M. McDermid, R. Morganti, T. Naab, T. Oosterloo, M. Sarzi, N. Scott, P. Serra, G. van de Ven, A.-M. Weijmans, and L. M. Young. The ATLAS^{3D} project - III. A census of the stellar angular momentum within the effective radius of early-type galaxies: unveiling the distribution of fast and slow rotators. *Monthly Notices of the Royal Astronomical Society*, 414:888–912, June 2011. doi: 10.1111/j.1365-2966.2011.18496.x.

Eric Emsellem, Michele Cappellari, Davor Krajnović, Glenn van de Ven, R. Bacon, M. Bureau, Roger L. Davies, P. T. de Zeeuw, Jesús Falcón-Barroso, Harald Kuntschner, Richard McDermid, Reynier F. Peletier, and Marc Sarzi. The SAURON project - IX. A kinematic classification for early-type galaxies. *Monthly Notices of the Royal Astronomical Society*, 379(2):401–417, Aug 2007. doi: 10.1111/j.1365-2966.2007.11752.x.

S. M. Faber, Scott Tremaine, Edward A. Ajhar, Yong-Ik Byun, Alan Dressler, Karl Gebhardt, Carl Grillmair, John Kormendy, Tod R. Lauer, and Douglas Richstone. The Centers of Early-Type Galaxies with HST. IV. Central Parameter Relations. *The Astronomical Journal*, 114:1771, Nov 1997. doi: 10.1086/118606.

Laura Ferrarese and David Merritt. A Fundamental Relation between Supermassive Black Holes and Their Host Galaxies. *The Astrophysical Journal*, 539(1):L9–L12, Aug 2000. doi: 10.1086/312838.

O. E. Gerhard. Line-of-sight velocity profiles in spherical galaxies: breaking the degeneracy between anisotropy and mass. *Monthly Notices of the Royal Astronomical Society*, 265:213, Nov 1993. doi: 10.1093/mnras/265.1.213.

Ortwin Gerhard, Gunther Jeske, R. P. Saglia, and Ralf Bender. Breaking the degeneracy between anisotropy and mass: the dark halo of the E0 galaxy NGC6703. *Monthly Notices of the Royal Astronomical Society*, 295(1):197–215, Mar 1998. doi: 10.1046/j.1365-8711.1998.29511341.x.

Charles F. Goullaud, Joseph B. Jensen, John P. Blakeslee, Chung-Pei Ma, Jenny E. Greene, and Jens Thomas. The MASSIVE Survey. IX. Photometric Analysis of 35 High-mass Early-type Galaxies with HST WFC3/IR. *The Astrophysical Journal*, 856(1):11, March 2018. doi: 10.3847/1538-4357/aab1f3.

Alister W. Graham. Core Depletion from Coalescing Supermassive Black Holes. *The Astrophysical Journal Letters*, 613(1):L33–L36, Sep 2004. doi: 10.1086/424928.

Alister W. Graham, Peter Erwin, I. Trujillo, and A. Asensio Ramos. A New Empirical Model for the Structural Analysis of Early-Type Galaxies, and A Critical Review of the Nuker Model. *The Astronomical Journal*, 125(6):2951–2963, Jun 2003. doi: 10.1086/375320.

Alessia Gualandris, Justin I. Read, Walter Dehnen, and Elisa Bortolas. Collisionless loss-cone refilling: there is no final parsec problem. *Monthly Notices of the Royal Astronomical Society*, 464(2):2301–2310, Jan 2017. doi: 10.1093/mnras/stw2528.

Lars Hernquist. An Analytical Model for Spherical Galaxies and Bulges. *The Astrophysical Journal*, 356:359, Jun 1990. doi: 10.1086/168845.

Philip F. Hopkins, Lars Hernquist, Thomas J. Cox, Suvendra N. Dutta, and Barry Rothberg. Dissipation and Extra Light in Galactic Nuclei. I. Gas-Rich Merger

Remnants. *The Astrophysical Journal*, 679(1):156–181, May 2008. doi: 10.1086/587544.

E. P. Hubble. Extragalactic nebulae. *The Astrophysical Journal*, 64:321–369, Dec 1926. doi: 10.1086/143018.

W. Jaffe. A simple model for the distribution of light in spherical galaxies. *Monthly Notices of the Royal Astronomical Society*, 202:995–999, Mar 1983. doi: 10.1093/mnras/202.4.995.

John Kormendy and Ralf Bender. The Double Nucleus and Central Black Hole of M31. *The Astrophysical Journal*, 522(2):772–792, Sep 1999. doi: 10.1086/307665.

John Kormendy and Luis C. Ho. Coevolution (Or Not) of Supermassive Black Holes and Host Galaxies. *Annual Review of Astronomy and Astrophysics*, 51(1):511–653, Aug 2013. doi: 10.1146/annurev-astro-082708-101811.

John Kormendy, David B. Fisher, Mark E. Cornell, and Ralf Bender. Structure and Formation of Elliptical and Spheroidal Galaxies. *The Astrophysical Journal Supplement Series*, 182(1):216–309, May 2009. doi: 10.1088/0067-0049/182/1/216.

Davor Krajnović, Michele Cappellari, P. Tim de Zeeuw, and Yannick Copin. Kinemetry: a generalization of photometry to the higher moments of the line-of-sight velocity distribution. *Monthly Notices of the Royal Astronomical Society*, 366(3):787–802, Mar 2006. doi: 10.1111/j.1365-2966.2005.09902.x.

Davor Krajnović, R. Bacon, Michele Cappellari, Roger L. Davies, P. T. de Zeeuw, Eric Emsellem, Jesús Falcón-Barroso, Harald Kuntschner, Richard M. McDermid, Reynier F. Peletier, Marc Sarzi, Remco C. E. van den Bosch, and Glenn van de Ven. The SAURON project - XII. Kinematic substructures in early-type galaxies:

evidence for discs in fast rotators. *Monthly Notices of the Royal Astronomical Society*, 390(1):93–117, Oct 2008. doi: 10.1111/j.1365-2966.2008.13712.x.

Davor Krajnović, Eric Emsellem, Michele Cappellari, Katherine Alatalo, Leo Blitz, Maxime Bois, Frédéric Bournaud, Martin Bureau, Roger L. Davies, Timothy A. Davis, P. T. de Zeeuw, Sadegh Khochfar, Harald Kuntschner, Pierre-Yves Lablanche, Richard M. McDermid, Raffaella Morganti, Thorsten Naab, Tom Oosterloo, Marc Sarzi, Nicholas Scott, Paolo Serra, Anne-Marie Weijmans, and Lisa M. Young. The ATLAS^{3D} project - II. Morphologies, kinemetric features and alignment between photometric and kinematic axes of early-type galaxies. *Monthly Notices of the Royal Astronomical Society*, 414(4):2923–2949, Jul 2011. doi: 10.1111/j.1365-2966.2011.18560.x.

Davor Krajnović, A. M. Karick, Roger L. Davies, Thorsten Naab, Marc Sarzi, Eric Emsellem, Michele Cappellari, Paolo Serra, P. T. de Zeeuw, Nicholas Scott, Richard M. McDermid, Anne-Marie Weijmans, Timothy A. Davis, Katherine Alatalo, Leo Blitz, Maxime Bois, Martin Bureau, Frederic Bournaud, Alison Crocker, Pierre-Alain Duc, Sadegh Khochfar, Harald Kuntschner, Raffaella Morganti, Tom Oosterloo, and Lisa M. Young. The ATLAS^{3D} Project - XXIII. Angular momentum and nuclear surface brightness profiles. *Monthly Notices of the Royal Astronomical Society*, 433(4):2812–2839, Aug 2013. doi: 10.1093/mnras/stt905.

T. R. Lauer, E. A. Ajhar, Y. I. Byun, A. Dressler, S. M. Faber, C. Grillmair, J. Kormendy, D. Richstone, and S. Tremaine. The Centers of Early-Type Galaxies with HST.I.An Observational Survey. *The Astronomical Journal*, 110:2622, Dec 1995. doi: 10.1086/117719.

Tod R. Lauer, S. M. Faber, Douglas Richstone, Karl Gebhardt, Scott Tremaine, Marc Postman, Alan Dressler, M. C. Aller, Alexei V. Filippenko, and Richard

Green. The Masses of Nuclear Black Holes in Luminous Elliptical Galaxies and Implications for the Space Density of the Most Massive Black Holes. *The Astrophysical Journal*, 662(2):808–834, Jun 2007a. doi: 10.1086/518223.

Tod R. Lauer, Karl Gebhardt, S. M. Faber, Douglas Richstone, Scott Tremaine, John Kormendy, M. C. Aller, Ralf Bender, Alan Dressler, and Alexei V. Filippenko. The Centers of Early-Type Galaxies with Hubble Space Telescope. VI. Bimodal Central Surface Brightness Profiles. *The Astrophysical Journal*, 664(1):226–256, July 2007b. doi: 10.1086/519229.

Chung-Pei Ma, Jenny E. Greene, Nicholas McConnell, Ryan Janish, John P. Blakeslee, Jens Thomas, and Jeremy D. Murphy. The MASSIVE Survey. I. A Volume-limited Integral-field Spectroscopic Study of the Most Massive Early-type Galaxies within 108 Mpc. *The Astrophysical Journal*, 795(2):158, Nov 2014. doi: 10.1088/0004-637X/795/2/158.

Matias Mannerkoski, Peter H. Johansson, Pauli Pihajoki, Antti Rantala, and Naab Thorsten. Inspiral of Supermassive Black Holes In Galactic Scale Simulations. *Monthly Notices of the Royal Astronomical Society*, 856(1):11, ? 2019. doi: 10.3847/1538-4357/aab1f3.

David Merritt. Mass Deficits, Stalling Radii, and the Merger Histories of Elliptical Galaxies. *The Astrophysical Journal*, 648(2):976–986, Sep 2006. doi: 10.1086/506139.

David Merritt. *Dynamics and Evolution of Galactic Nuclei*. 2013.

Miloš Milosavljević and David Merritt. Formation of Galactic Nuclei. *The Astrophysical Journal*, 563(1):34–62, Dec 2001. doi: 10.1086/323830.

Miloš Milosavljević and David Merritt. The Final Parsec Problem. In Joan M. Centrella, editor, *The Astrophysics of Gravitational Wave Sources*, volume 686 of

American Institute of Physics Conference Series, pages 201–210, Oct 2003. doi: 10.1063/1.1629432.

Miloš Milosavljević, David Merritt, Armin Rest, and Frank C. van den Bosch. Galaxy cores as relics of black hole mergers. *Monthly Notices of the Royal Astronomical Society*, 331(4):L51–L55, Apr 2002. doi: 10.1046/j.1365-8711.2002.05436.x.

Houjun Mo, Frank C. van den Bosch, and Simon White. *Galaxy Formation and Evolution*. 2010.

Thorsten Naab and Andreas Burkert. Statistical Properties of Collisionless Equal- and Unequal-Mass Merger Remnants of Disk Galaxies. *The Astrophysical Journal*, 597(2):893–906, Nov 2003. doi: 10.1086/378581.

Thorsten Naab, Sadegh Khochfar, and Andreas Burkert. Properties of Early-Type, Dry Galaxy Mergers and the Origin of Massive Elliptical Galaxies. *The Astrophysical Journal Letters*, 636(2):L81–L84, Jan 2006. doi: 10.1086/500205.

Thorsten Naab, Peter H. Johansson, and Jeremiah P. Ostriker. Minor Mergers and the Size Evolution of Elliptical Galaxies. *The Astrophysical Journal Letters*, 699 (2):L178–L182, Jul 2009. doi: 10.1088/0004-637X/699/2/L178.

J. A. Nelder and R. Mead. A Simplex Method for Function Minimization. *The Computer Journal*, 7(4):308–313, 01 1965. ISSN 0010-4620. doi: 10.1093/comjnl/7.4.308. URL https://doi.org/10.1093/comjnl/7.4.308.

Ludwig Oser, Jeremiah P. Ostriker, Thorsten Naab, Peter H. Johansson, and Andreas Burkert. The Two Phases of Galaxy Formation. *The Astrophysical Journal*, 725(2):2312–2323, Dec 2010. doi: 10.1088/0004-637X/725/2/2312.

Gerald D. Quinlan and Lars Hernquist. The dynamical evolution of massive black hole binaries — II. Self-consistent N-body integrations. *New Astronomy*, 2(6): 533–554, Dec 1997. doi: 10.1016/S1384-1076(97)00039-0.

Antti Rantala, Peter H. Johansson, Thorsten Naab, Jens Thomas, and Matteo Frigo. The Formation of Extremely Diffuse Galaxy Cores by Merging Supermassive Black Holes. *The Astrophysical Journal*, 864(2):113, September 2018. doi: 10.3847/1538-4357/aada47.

Antti Rantala, Peter H. Johansson, Thorsten Naab, Jens Thomas, and Matteo Frigo. The Simultaneous Formation of Cored, Tangentially Biased, and Kinematically Decoupled Centers in Massive Early-type Galaxies. *The Astrophysical Journal Letters*, 872(2):L17, Feb 2019. doi: 10.3847/2041-8213/ab04b1.

C. Rodriguez, G. B. Taylor, R. T. Zavala, A. B. Peck, L. K. Pollack, and R. W. Romani. A Compact Supermassive Binary Black Hole System. *The Astrophysical Journal*, 646(1):49–60, Jul 2006. doi: 10.1086/504825.

S. P. Rusli, P. Erwin, R. P. Saglia, J. Thomas, M. Fabricius, R. Bender, and N. Nowak. Depleted Galaxy Cores and Dynamical Black Hole Masses. *The Astronomical Journal*, 146(6):160, Dec 2013a. doi: 10.1088/0004-6256/146/6/160.

S. P. Rusli, J. Thomas, R. P. Saglia, M. Fabricius, P. Erwin, R. Bender, N. Nowak, C. H. Lee, A. Riffeser, and R. Sharp. The Influence of Dark Matter Halos on Dynamical Estimates of Black Hole Mass: 10 New Measurements for High-σ Early-type Galaxies. *The Astronomical Journal*, 146(3):45, Sep 2013b. doi: 10.1088/0004-6256/146/3/45.

R. P. Saglia, M. Opitsch, P. Erwin, J. Thomas, A. Beifiori, M. Fabricius, X. Mazzalay, N. Nowak, S. P. Rusli, and R. Bender. The SINFONI Black Hole Survey: The Black Hole Fundamental Plane Revisited and the Paths of (Co)evolution of

Supermassive Black Holes and Bulges. *The Astrophysical Journal*, 818(1):47, Feb 2016. doi: 10.3847/0004-637X/818/1/47.

Thomas S. Statler. Is the Kinematically Distinct Core in NGC 5982 Necessarily the Remnant of an Accreted Companion? *The Astrophysical Journal Letters*, 382: L11, Nov 1991. doi: 10.1086/186202.

Jose Luis Sérsic. *Atlas de Galaxias Australes*. 1968.

J. Thomas, R. P. Saglia, R. Bender, D. Thomas, K. Gebhardt, J. Magorrian, E. M. Corsini, and G. Wegner. Dynamical modelling of luminous and dark matter in 17 Coma early-type galaxies. *Monthly Notices of the Royal Astronomical Society*, 382(2):657–684, Dec 2007. doi: 10.1111/j.1365-2966.2007.12434.x.

J. Thomas, R. P. Saglia, R. Bender, P. Erwin, and M. Fabricius. The Dynamical Fingerprint of Core Scouring in Massive Elliptical Galaxies. *The Astrophysical Journal*, 782(1):39, Feb 2014. doi: 10.1088/0004-637X/782/1/39.

Jens Thomas, Chung-Pei Ma, Nicholas J. McConnell, Jenny E. Greene, John P. Blakeslee, and Ryan Janish. A 17-billion-solar-mass black hole in a group galaxy with a diffuse core. *Nature*, 532(7599):340–342, April 2016. doi: 10.1038/nature17197.

Roeland P. van der Marel and Marijn Franx. A New Method for the Identification of Non-Gaussian Line Profiles in Elliptical Galaxies. *The Astrophysical Journal*, 407:525, Apr 1993. doi: 10.1086/172534.

Melanie Veale, Chung-Pei Ma, Jens Thomas, Jenny E. Greene, Nicholas J. McConnell, Jonelle Walsh, Jennifer Ito, John P. Blakeslee, and Ryan Janish. The MASSIVE Survey - V. Spatially resolved stellar angular momentum, velocity dispersion, and higher moments of the 41 most massive local early-type galaxies.

Monthly Notices of the Royal Astronomical Society, 464(1):356–384, January 2017. doi: 10.1093/mnras/stw2330.

Melanie Veale, Chung-Pei Ma, Jenny E. Greene, Jens Thomas, John P. Blakeslee, Jonelle L. Walsh, and Jennifer Ito. The MASSIVE survey - VIII. Stellar velocity dispersion profiles and environmental dependence of early-type galaxies. *Monthly Notices of the Royal Astronomical Society*, 473(4):5446–5467, February 2018. doi: 10.1093/mnras/stx2717.

P. Young. Numerical models of star clusters with a central black hole. I - Adiabatic models. *The Astrophysical Journal*, 242:1232–1237, Dec 1980. doi: 10.1086/158553.

Marcel Zemp, Oleg Y. Gnedin, Nickolay Y. Gnedin, and Andrey V. Kravtsov. On Determining the Shape of Matter Distributions. *The Astrophysical Journal Supplement*, 197(2):30, December 2011. doi: 10.1088/0067-0049/197/2/30.